Solid-state NMR spectroscopy

Bernd Reif[1], Sharon E. Ashbrook[2], Lyndon Emsley [3] and Mei Hong [4] ✉

Abstract | Solid-state nuclear magnetic resonance (NMR) spectroscopy is an atomic-level method to determine the chemical structure, 3D structure and dynamics of solids and semi-solids. This Primer summarizes the basic principles of NMR spectroscopy as applied to the wide range of solid systems. The nuclear spin interactions and the effects of magnetic fields and radiofrequency pulses on nuclear spins in solid-state NMR are the same as in liquid-state NMR spectroscopy. However, because of the orientation dependence of the nuclear spin interactions in the solid state, the majority of high-resolution solid-state NMR spectra are measured under magic-angle spinning (MAS), which has profound effects on the types of radiofrequency pulse sequences required to extract structural and dynamical information. We describe the most common MAS NMR experiments and data analysis approaches for investigating biological macromolecules, organic materials and inorganic solids. Continuing development of sensitivity-enhancement NMR approaches, including ¹H-detected fast MAS experiments, dynamic nuclear polarization and experiments in ultra-high magnetic fields, is described. We highlight recent applications of solid-state NMR spectroscopy to biological and materials chemistry. The Primer ends with a discussion of current limitations as well as areas of development of solid-state NMR spectroscopy and points to emerging areas of applications of this sophisticated spectroscopy.

Non-zero nuclear spins
Nuclear isotopes with a non-zero spin angular momentum.

Gyromagnetic ratio
The ratio of the magnetic moment of a particle to its angular momentum.

Anisotropic
Orientation-dependent.

[1]*Technische Universität München, Department Chemie, Garching, Germany.*

[2]*School of Chemistry, University of St Andrews, St Andrews, UK.*

[3]*École Polytechnique Fédérale de Lausanne (EPFL), Institut des sciences et ingénierie chimiques, Lausanne, Switzerland.*

[4]*Department of Chemistry and Francis Bitter Magnet Laboratory, Massachusetts Institute of Technology, Cambridge, MA, USA.*

✉*e-mail: meihong@mit.edu*

https://doi.org/10.1038/s43586-020-00002-1

Nuclear magnetic resonance (NMR) spectroscopy probes the chemical structrure, three-dimensional structure and motion of molecules and materials. NMR is the oscillatory response of nuclei with non-zero spins in a magnetic field to resonant excitation by radiofrequency irradiation. When atoms containing non-zero nuclear spins (TABLE 1) are placed in an external magnetic field, the degeneracy of the nuclear spin states is lifted, leading to an energy difference ΔE given by Eq. (1):

$$\Delta E = \gamma \hbar (1 - \sigma) B_0 \tag{1}$$

where γ is the gyromagnetic ratio, a fundamental property associated with each isotope; B_0 is the strength of the static magnetic field; and σ is the chemical shielding around a nucleus. Transitions can then be induced by electromagnetic radiation between these nuclear spin states[1] (FIG. 1). With typical magnetic fields of 5–28 T used in NMR spectroscopy today, the transition frequencies lie in the radiofrequency regime of the electromagnetic spectrum (213–1200 MHz ¹H Larmor frequencies). The NMR transition frequencies are sensitive to the electron distribution around the nucleus, which shields the nucleus from the applied magnetic field. The shielding constant, σ, varies for different nuclei of a given isotope in a molecule, causing slightly different frequencies. Thus, NMR frequencies reveal the chemical structure of the sample[2,3]. NMR frequencies are commonly reported as a chemical shift, δ, which is the fractional difference between the frequency of a particular nucleus and a standard compound such as tetramethylsilane. For a given isotope, chemical shift differences can range from 10 parts per million (ppm) for ¹H to 200 ppm for ¹³C to 1,000 ppm for ¹⁷O. In addition to chemical shifts, NMR frequencies are modified by a series of couplings: spin–spin scalar couplings, which depend on covalent bonding and are typically in the 0–1 kHz range; spin–spin dipolar couplings, which depend on internuclear distances and are typically in the 0–20 kHz range; and, for nuclear spins greater than 1/2, quadrupolar couplings between the electric field gradient at the nucleus and the charge distribution of the nucleus, which range from 100 kHz to tens of megahertz. All of these NMR interactions are anisotropic, that is, they depend on the sample orientation relative to the magnetic field direction. Because of these orientation-dependent chemical shifts, internuclear couplings and quadrupolar couplings, NMR spectra encode 3D structural information. Molecular rotations partially average these anisotropic interactions; thus, measurement of motionally averaged NMR spectra and motionally induced nuclear spin relaxation reveals the geometries and rates of motion.

The radiofrequency regime of the electromagnetic spectrum is orders of magnitude lower in frequency than the microwave, infrared and ultraviolet frequencies employed in rotational, vibrational and electronic

Table 1 | **Commonly studied nuclei in solid-state NMR spectroscopy**

Nuclei	Spin quantum number	Natural abundance (%)	NMR transition frequency at 18.8 T (MHz)	Examples of applications
^1H	1/2	99.98	800	Organic materials, proteins, lipids, energy materials
^{19}F	1/2	100	753	Organic materials, proteins, pharmaceutical compounds, minerals
^{31}P	1/2	100	324	Phospholipids, nucleic acids, phosphate frameworks
^7Li	3/2	92.6	311	Lithium ion batteries
^{27}Al	5/2	100	208	Aluminosilicate zeolites and minerals, phosphate frameworks
^{13}C	1/2	1.1	200	Organic and biological compounds, metal–organic frameworks
^{29}Si	1/2	4.7	159	Zeolites, minerals, silica catalysts
^2H	1	0.015	123	Water, carbohydrates, proteins, medicinal compounds
^{17}O	5/2	0.037	108	Water, carbohydrates, proteins, oxides, ceramics, catalysts
^{15}N	1/2	0.37	80	Proteins, nucleic acids, heterocyclic compounds, nitride ceramics

NMR, nuclear magnetic resonance.

spectroscopies. The low NMR frequencies entail that the energy levels of nuclear spins are nearly equally populated at room temperature, according to the Boltzmann distribution in Eq. (2):

$$\frac{N_+}{N_-} = e^{-\Delta E/kT} = e^{-\gamma\hbar(1-\sigma)B_0/kT} \qquad (2)$$

For example, at room temperature in a 10 T magnetic field, the population of the ground state (N_+) is in excess to that of the upper state (N_-) by only 1 in 10,000. This small population difference leads to intrinsically weak NMR signals and, hence, low signal-to-noise ratios in the spectra. These weak signals put stringent constraints on NMR sample volumes, methods of detection and instrumentation. Much of the development of modern NMR spectroscopy has focused on increasing sensitivity. One approach is to use higher magnetic fields to increase ΔE, which has been very successful, but this is limited by both technology and cost. Another approach is to record NMR spectra in the time domain following a radiofrequency pulse and obtain the spectrum by Fourier transformation rather than by sweeping the frequency and measuring absorption or emission as in classical spectroscopy[1,4]. With pulsed Fourier transformation NMR spectroscopy, one can sum the time-domain signals of many acquisitions to increase the signal-to-noise ratio of the NMR spectra. The introduction of pulsed Fourier transformation NMR spectroscopy increased the sensitivity of NMR by an order of magnitude and opened the avenue to multidimensional NMR spectroscopy. Further background for these fundamental aspects of modern NMR spectroscopy is outside the scope of this Primer, and the reader is referred to many excellent introductory textbooks such as those by Keeler[4] and Levitt[1]. The lower frequencies of NMR, although causing low sensitivity, give the important advantages that

NMR experiments are non-destructive and nuclear spin coherence times can be very long (up to seconds). This long coherence time permits the study of slow molecular motions and the design of sophisticated trains of radiofrequency pulses, whose exact timing and phases can be controlled to extract highly specific structural and dynamical information.

The application of NMR spectroscopy to rigid or semi-rigid solid samples spans an inexhaustible variety of systems, from membrane proteins and amyloid fibrils in biochemistry to polymers, battery materials, photovoltaic perovskites and cements in chemistry and materials sciences. In solids, the orientation dependence of NMR frequencies causes powder patterns for each nuclear spin. In most cases, this anisotropic contribution needs to be removed to obtain site-resolved spectra. This is accomplished by magic-angle spinning (MAS), where samples are physically spun around an axis that is tilted by 54.7° from the static magnetic field[5,6] (FIG. 1c). This angle results from the fact that the anisotropy of NMR interactions is given by a second-rank tensor, whose time average vanishes at 54.7°. Today, MAS rates of 5–100 kHz are accessible using cylindrical rotors with diameters ranging from 7 mm to 0.7 mm. Faster MAS averages out stronger anisotropic interactions. Currently, the vast majority of solid-state NMR experiments are carried out under MAS. Because MAS averages out the information-rich anisotropic chemical shift and dipolar interactions, many radiofrequency pulse sequences have been designed to selectively reintroduce the desired spin interactions while retaining spectral resolution, Such multi-pulse and multidimensional experiments are the basis of many modern solid-state NMR experiments[2,7].

Modern NMR spectra are obtained from Fourier transformation of the time-domain responses of the nuclear spins to radiofrequency pulses. In the simplest

Fourier transformation
A mathematical transformation that decomposes a function (usually of time) into its constituent frequencies.

case, a single pulse is followed by acquisition of a time-domain signal that decays to equilibrium in microseconds to seconds. However, multiple pulses can be applied sequentially in so-called pulse sequences, whose timings can be adjusted to precisely control the dynamics of the nuclear spins (Experimentation)[1,2,7]. These pulse sequences can be designed to average out certain nuclear spin interactions while retaining others. Pulse sequence elements can be combined in an almost unlimited number of configurations to allow the measurement of a wide array of multidimensional correlation spectra. As a result, multidimensional NMR spectroscopy can be tailored to a given chemical system to yield precise information about interatomic interactions that cannot be obtained from other structural techniques. The detailed design of multi-pulse multidimensional NMR experiments is outside the scope of this Primer and is treated elsewhere[2,7]. By understanding the nuclei whose frequencies are being correlated and the mechanism of correlation, whether through bonds or through space, users can readily apply these robust multidimensional

correlation NMR experiments to obtain information about chemical structure and 3D structure.

The interpretation of NMR spectra can be less intuitive than microscopy or diffraction data, because structural information is encoded in frequency spectra rather than spatial density maps. The frequency peaks need to be assigned to individual atoms, which can be a significant challenge. However, the multitude of peaks in NMR spectra represent an exquisite chemical fingerprint of molecules, thus making NMR spectroscopy the eye of chemists. The chemical shifts and couplings in the NMR spectra also contain 3D structural and dynamical information, thus revealing the mechanisms of action of biological and chemical systems.

This Primer describes the most common solid-state NMR experiments with their accompanying pulse sequences (Experimentation). We discuss how solid-state NMR spectra and data are interpreted (Results). We then highlight recent applications of solid-state NMR spectroscopy to biomolecular and materials chemistry (Applications). This is followed by a description of
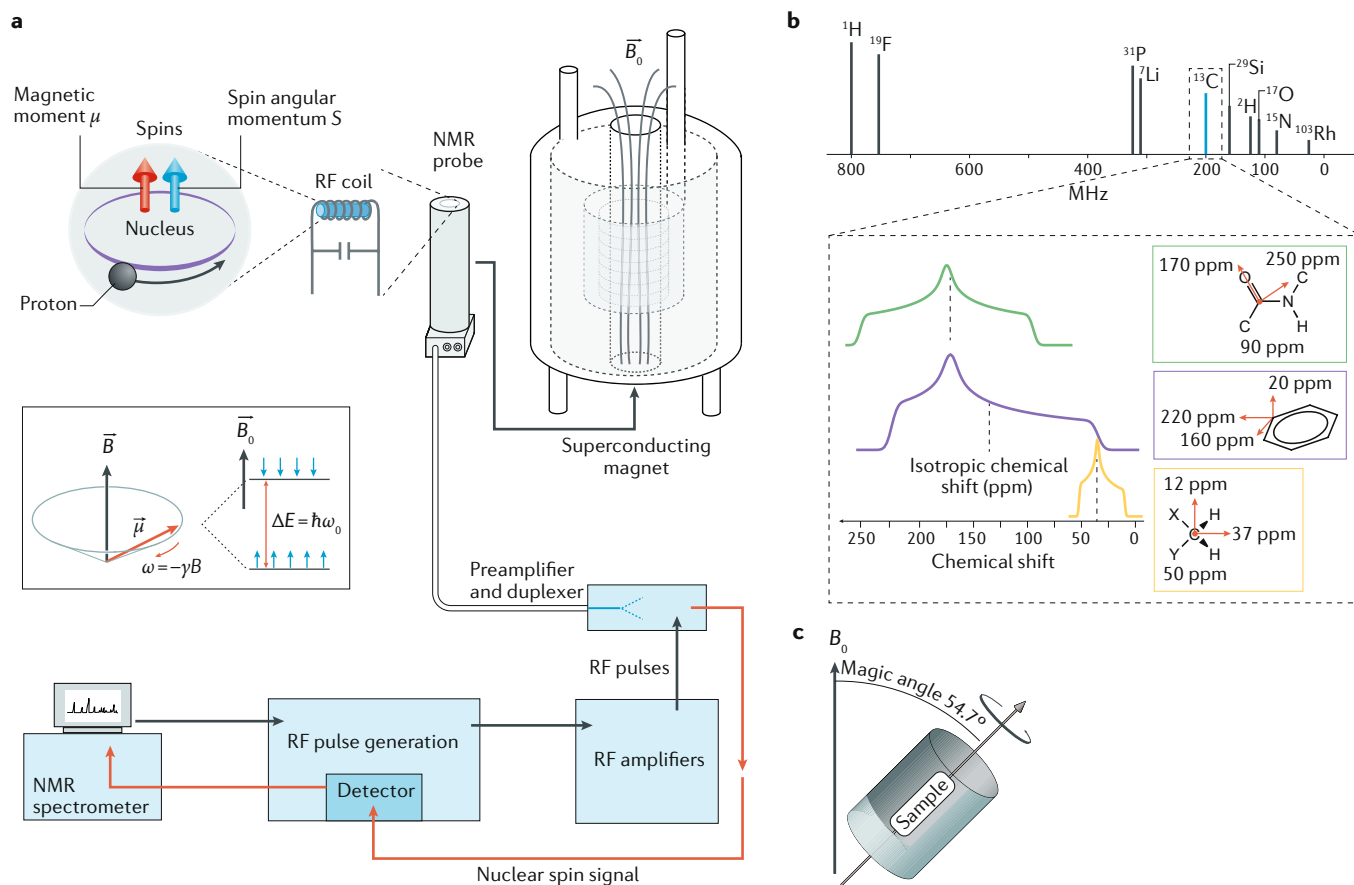

Fig. 1 | **Basics of solid-state NMR spectroscopy for structural analysis of biomolecules and materials. a** | Nuclear spin magnetic dipole moments (μ) precess around a static magnetic field (B_0) at a frequency identical to the transition frequency between the energy levels of the spins ($\Delta E = \hbar\omega_0$). A radiofrequency (RF) coil is wrapped around the sample at the top of a nuclear magnetic resonance (NMR) probe, which is inserted into the centre of the magnet. The RF coil allows irradiation of the RF pulses as well as detection of the transition frequency of the nuclear magnetic moment. Angular velocity, $\omega = -\gamma B$. **b** | The NMR frequencies of different nuclear isotopes depend on their gyromagnetic ratios (γ) and the magnetic field

($B_0 = 18.8$ T, in this example). In addition, for spins of the same isotope, the frequency depends on the electronic environment of the individual nuclei. Schematic NMR spectra of a static powder containing three ^{13}C nuclei report the chemical structure of the functional groups. The broad powder pattern reflects chemical shift anisotropy, whose geometric average corresponds to the isotropic chemical shift, which is detected when the sample undergoes magic-angle spinning (MAS). **c** | MAS of the sample in the rotor yields high-resolution NMR spectra of solids by averaging the anisotropic part of the interaction to zero. ppm, parts per million.

common guidelines for data sharing, reproducibility and reporting standards (Reproducibility and data deposition) and a discussion of the current limitations of solid-state NMR spectroscopy as well as areas of active advances (Limitations and optimizations). Finally, we look into the future of solid-state NMR spectroscopy and point out new and exciting areas of potential applications (Outlook).

Experimentation

In the following, we discuss the key steps involved in carrying out a solid-state NMR experiment. Specifically, this consists of sample preparation, experimental set-up, acquisition of NMR spectra, spectral assignment, and the choice of experiments to measure structural and dynamic parameters. The experimental choices are tailored to the systems of interest and guided by sensitivity considerations.

Sample preparation and isotopic enrichment

Many solid-state NMR spectra are recorded on unmodified samples at natural isotopic abundance. A major advantage of NMR spectroscopy is the ability to analyse samples in their native states, including powders, pastes, gels, fibrils and membranes, all of which do not have to be crystalline.

Samples are directly packed or centrifuged into the sample holders, which are usually airtight and watertight ceramic rotors for MAS experiments. Thus, air-sensitive and hydrated samples can be studied. The rotors are cylinders that typically have outer diameters of 7, 4, 3.2, 2.5, 1.3 or 0.7 mm, which can accommodate between 500 mg (for 7 mm) and 1 mg (for 0.7 mm) of sample. Small rotors are used for higher MAS speeds (~100 kHz for 0.7 mm) whereas larger rotors are used for lower MAS speeds (~5 kHz for 7 mm).

Depending on the nature of the sample, isotopic enrichment can be paramount for obtaining high spectral sensitivity, as many NMR-active nuclei occur at low natural abundance (TABLE 1). Various ^{13}C and ^{15}N-enriched biological compounds, such as amino acids and sugars, are commercially available. Proteins can be uniformly or site-specifically ^{13}C and ^{15}N-enriched using such precursors during recombinant bacterial expression[8–10]. Proteins can also be perdeuterated and back-exchanged with protonated solvent to allow ^1H-detected fast MAS experiments for structure determination and ^2H NMR experiments for dynamics investigations. In addition to enhancing spectral sensitivity, isotopic enrichment distinguishes the molecule of interest from the unlabelled matrix. For example, ^{13}C and ^{15}N-labelled membrane proteins can be distinguished from unlabelled phospholipids, and ^{13}C and ^{15}N-labelled amyloid proteins can be distinguished from unlabelled brain tissues[11].

In materials chemistry, ^{29}Si is commonly enriched using tetraethyl orthosilicate, whereas ^{17}O is commonly enriched using gaseous $^{17}O_2$ and liquid $H_2^{17}O$ (REF.[12]). The high cost of ^{17}O-enriched reagents has motivated the development of more efficient synthetic approaches such as high-temperature exchange with oxygen gas, ionothermal synthesis[12], dry gel conversion reactions, small-scale hydrolysis and mechanochemistry.

1D and 2D correlation NMR

NMR spectroscopists apply multiple radiofrequency pulses with specific timings, phases and amplitudes (FIG. 2) to manipulate the nuclear magnetic moments in order to obtain the structural information of interest. The first, and simplest, experiment for analysing most samples is a 1D MAS experiment involving either direct excitation of the nuclear spin or cross-polarization from protons (CPMAS)[6,13] (FIG. 2a). CPMAS is the workhorse experiment for ^1H-rich organic compounds because it enhances the signal sensitivity of a rare and low-γ nucleus X (any nucleus other than ^1H) by transferring magnetization from the abundant and high-γ protons. ^1H decoupling (BOX 1) is applied during X-nucleus detection to enhance spectral resolution. 1D CPMAS spectra show one peak for each chemically distinct site. At moderate MAS rates (<20 kHz), sites with large chemical shift anisotropies (CSAs) exhibit spinning sidebands, whose intensities can be fitted to extract the principal values of the CSA tensor[3,14]. At conventional MAS rates (up to about 50 kHz), ^1H solid-state NMR spectra of organic compounds cannot be directly detected owing to the line broadening caused by multi-spin ^1H–^1H dipolar couplings. Instead, they can be measured in the indirect dimension of 2D correlation spectra by applying ^1H–^1H homonuclear decoupling sequences[15–18]. At ultrafast MAS rates of ~100 kHz, the ^1H linewidths narrow sufficiently that high-resolution ^1H spectra can be measured directly[19].

A core strength of NMR spectroscopy is the ability to produce versatile and structurally informative multidimensional correlation spectra. In materials chemistry, the most widely used 2D solid-state NMR experiment is heteronuclear chemical shift correlation (HETCOR) (FIG. 2b), particularly involving ^1H. The correlation is mediated by either through-bond J coupling or through-space dipolar coupling (BOX 1). ^1H correlation to ^{13}C, ^{29}Si, ^{31}P and other nuclei has been widely applied. HETCOR experiments can also be conducted for non-proton spins, provided that the NMR probe can be tuned to the two frequencies of interest.

Homonuclear 2D correlation NMR spectra also contain rich information. When both dimensions encode isotropic chemical shifts, which are referred to as single-quantum shifts, the spectra report conformational dynamics, chemical exchange and spatial proximities[20] (FIG. 2c). Alternatively, homonuclear 2D NMR spectra can be measured by correlating the single-quantum chemical shifts of each nucleus with the sum chemical shift of two nuclei, which are manifested by double-quantum coherence between the two spins (FIG. 2d). This incredible natural abundance double-quantum transfer experiment (INADEQUATE)[21], adapted for spinning solids[22], has been applied to many nuclei such as ^{13}C, ^{31}P and ^{29}Si to determine the structure of pharmaceutical compounds[23], network structures in phosphates[24] and structure distributions in materials such as cellulose[25].

A third class of 2D solid-state NMR experiments correlates an anisotropic interaction such as CSA and dipolar coupling with the isotropic chemical shift. The anisotropic interaction is usually recoupled under MAS by rotor-synchronized pulses. Dipolar recoupling (BOX 1) is the basis of many modern solid-state NMR
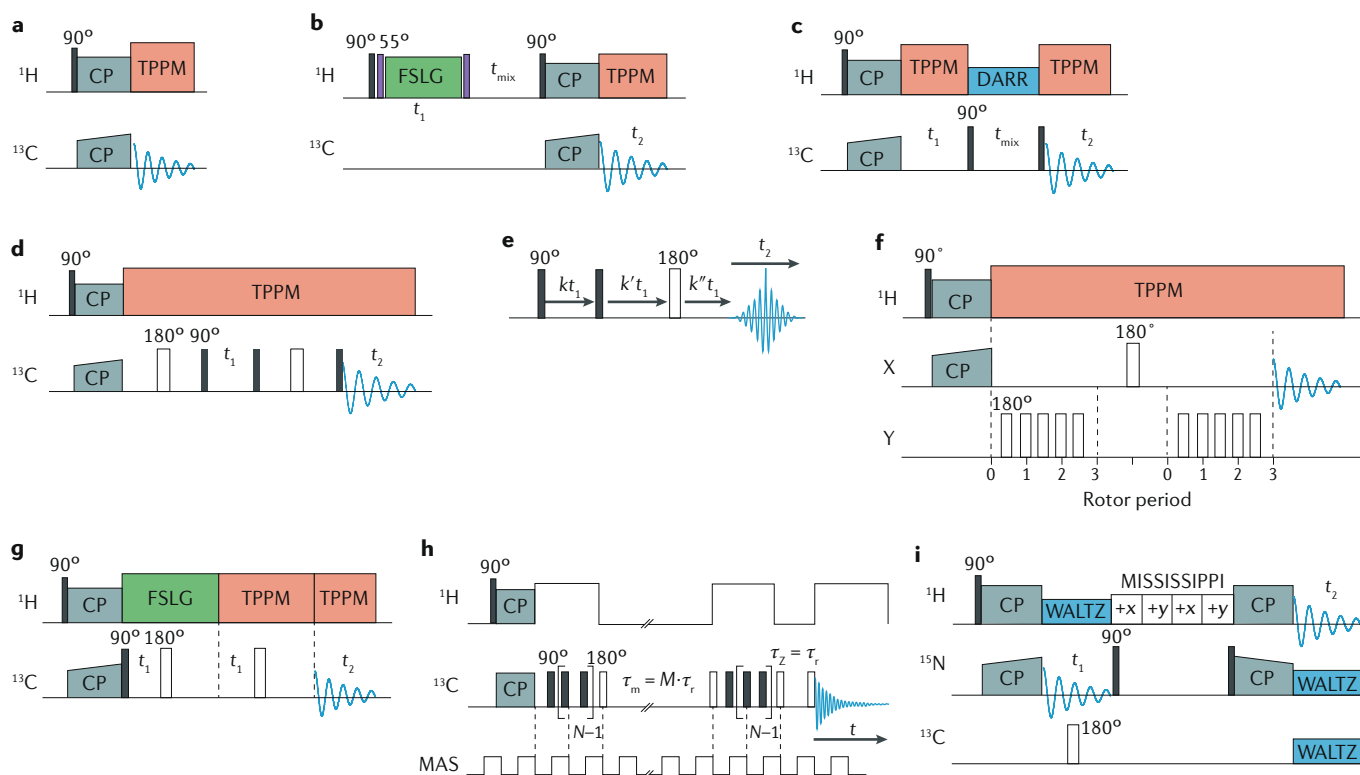
Fig. 2 | **Some common solid-state NMR pulse sequences.** ^{13}C is used as an example of a heteronuclear (X) spin. **a** | Cross-polarization (CP). **b** | 2D ^{1}H–^{13}C heteronuclear chemical shift correlation (HETCOR) with ^{1}H homonuclear decoupling. **c** | 2D ^{13}C–^{13}C correlation through dipolar spin diffusion. **d** | 2D ^{13}C–^{13}C J-based refocused incredible natural abundance double quantum transfer experiment (INADEQUATE). **e** | Multiple-quantum magic-angle spinning (MQMAS) experiment for quadrupolar nuclei. **f** | X–Y rotational echo double resonance (REDOR) for heteronuclear distance measurement. **g** | 2D ^{13}C–^{1}H dipolar-shift correlation (DIPSHIFT). **h** | Centreband-only detection of exchange (CODEX) pulse sequence for studying slow motion. **i** | 2D ^{1}H-detected hNH correlation under fast MAS. A broad-band composite pulse decoupling scheme (WALTZ) is applied to yield heteronuclear scalar decoupling. In these pulse sequences, the heteronuclear decoupling scheme can be two-pulse phase modulation (TPPM), SPINAL (a decoupling sequence extension of TPPM) and other sequences, whereas the homonuclear decoupling scheme can be frequency-switched Lee–Goldburg (FSLG), a numerically optimized sequence (DUMBO) and other sequences. t_1 and t_2 refer to time-domain increments for 2D and 3D experiments, and 90° and 180° pulses are shown as filled and open narrow rectangles, respectively. DARR, dipolar-assisted rotational resonance; MISSISSIPPI, Multiple Intense Solvent Suppression Intended for Sensitive Spectroscopic Investigation of Protonated Proteins, Instantly; M, N, numbers of rotor periods; NMR, nuclear magnetic resonance; t_{mix}, mixing time; τ_m, mixing time; τ_r, rotor period; τ_Z, z-filter period.

experiments[26]. Anisotropic interactions can also be measured by switching the rotor axis away from the magic angle[27,28]. However, this variable-angle spinning approach is now less common owing to its requirement for specialized probes.

Unlike spin-1/2 nuclei, solid-state NMR spectra of quadrupolar nuclei (spin >1/2) are usually megahertz wide because of the large size of quadrupolar interactions[29,30]. This quadrupolar broadening is inversely proportional to the magnetic field strength; thus, high magnetic fields are advantageous for obtaining high-resolution spectra of quadrupolar nuclei[31]. MAS removes quadrupolar broadening to first order; but significant sidebands remain at moderate spinning rates. Moreover, when the quadrupolar interaction is large, its effect needs to be considered to second order, which cannot be averaged by MAS due to additional higher-order angular dependence. The most common method for removing the quadrupolar broadening is the multiple-quantum MAS (MQMAS) experiment[32], which correlates different transitions within the spin system and yields an isotropic spectrum from the projection onto the indirect dimension (FIG. 2e). When the quadrupolar broadening is too large even for MQMAS to overcome, 1D 'wideline' NMR spectra are measured for static samples (i.e. with no sample rotation) as a series of sub-spectra[33], each measured with different frequency offsets to yield an undistorted line shape.

Unlike most half-integer quadrupolar nuclei, ^{2}H is a spin-1 nucleus whose NMR spectra are relatively simple to measure because of the small quadrupolar coupling constant (~200 kHz) and the relative ease of deuteration. Both static and MAS ^{2}H NMR spectra can be measured using the two-pulse quadrupolar echo sequence. ^{2}H solid-state NMR spectra are often measured in specifically deuterated systems as a function of temperature to extract the geometry, rates and energetics of molecular motion. Static ^{2}H NMR spectroscopy has been widely applied to study polymer dynamics[2,34] and lipid membrane dynamics[35]. For the latter, acyl chain order parameters can be quantified in the absence and presence of proteins using chain-perdeuterated lipids[36,37]. Recently, ^{13}C and ^{15}N-detected ^{2}H MAS NMR experiments have been indirectly developed to study uniformly labelled proteins and carbohydrates to determine molecular motion in a site-resolved and multiplexed manner[38–40].

3D correlation NMR

For ^{13}C and ^{15}N-labelled proteins, a number of 2D and 3D correlation experiments are now well established for measuring the ^{13}C and ^{15}N chemical shifts and assigning them to specific amino acid residues. For resonance assignment of small proteins (<20 kDa) that have high structural homogeneity, 2D ^{13}C–^{13}C and ^{15}N–^{13}C correlation spectra are usually measured first to serve as fingerprints of the protein conformation. Three 3D ^{15}N–^{13}C correlation experiments — intra-residue NCACX, inter-residue NCOCX and inter-residue CONCA — are then conducted to obtain the sequence-specific assignment[41] (for the correlation patterns measured, see FIG. 3a). For larger proteins, low spectral sensitivity limits the applicability of these ^{13}C-detected 3D experiments, thus ^{1}H-detected 3D experiments are increasingly used instead. These ^{1}H-detected experiments are usually conducted on perdeuterated proteins for MAS rates of less than 60 kHz and protonated proteins for MAS rates of 100 kHz or above. Perdeuteration reduces the ^{1}H density whereas 100 kHz MAS yields highly efficient averaging of the ^{1}H–^{1}H dipolar coupling, both yielding high-resolution ^{1}H spectra. These ^{1}H-detected NMR experiments use either J couplings or dipolar couplings to mediate spin polarization transfer[19,42,43]. The long coherence lifetimes at the fastest MAS rates make certain J-based polarization transfer steps the most efficient[44–46]. Higher-dimensional (4D, 5D) experiments have also been proposed that employ automated projection spectroscopy[47] and non-uniform sampling[48,49] to produce peak lists from lower-order spectra[50], and enable semi-automated resonance assignment[51–53].

Distance measurement

Interatomic distances (through space) can be measured in NMR spectroscopy through the effect of spin–spin dipolar couplings. Qualitative inter-proton or inter-carbon distance restraints can be obtained from cross-peak intensities in spin diffusion-mediated multi-dimensional correlation spectra. Weak and strong cross-peaks indicate long and short distances, respectively[54]. In biomolecules, ^{1}H–^{1}H or ^{13}C–^{13}C distances are commonly measured via 2D ^{13}C–^{13}C or ^{13}C–^{15}N planes in 3D correlation spectra and are used to derive short, medium and long distance restraints[44,55,56]. This yields distance restraints on the order of <7 Å for ^{13}C–^{13}C (REF.[55]), <13 Å for ^{1}H–^{1}H (REF.[57]) and <16 Å for ^{19}F–^{19}F (REF.[58]) distances.

Heteronuclear distances can be measured precisely using the rotational-echo double-resonance (REDOR) experiment[59] (FIG. 2f), which is one of the most versatile and robust techniques in solid-state NMR spectroscopy. The experiment uses a train of 180° pulses spaced half a rotor period apart to reintroduce heteronuclear dipolar couplings that would otherwise be averaged by MAS. There are many variants of the REDOR experiment, but usually, two experiments with (S) and without (S_0) 180° pulses on the unobserved channel are conducted, and the resulting intensities are divided (S/S_0) to yield relaxation-free dipolar dephasing curves. These dephasing curves have a universal shape regardless of the coupling strengths, and differ only in the modulation time. REDOR has been applied to a large number of spin pairs[60], such as ^{13}C–^{15}N (REF.[61]), ^{13}C–^{31}P (REF.[62]) and ^{13}C–^{19}F (REFS[63,64]) in organic compounds and ^{27}Al–^{31}P, ^{27}Al–^{1}H (REF.[65]) and ^{17}O–^{1}H (REF.[66]) in inorganic compounds.

Nuclear spin dipolar couplings depend not only on internuclear distances but also on the gyromagnetic ratio γ of the spins. High-γ nuclei give stronger dipolar couplings, and thus their distances are easier to measure. REDOR between the high-γ ^{19}F and other nuclei such as ^{13}C and ^{1}H has recently been extended to high-field fast MAS conditions and has been incorporated into 2D experiments to obtain many nanometre-range distances rapidly[67,68]. Similarly, 2D ^{19}F–^{19}F correlation spectra under fast MAS have been developed to obtain cross-peaks indicative of distances up to ~2 nm (REFS[58,69–71]).

Studying molecular motion

Solid-state NMR spectroscopy is ideally suited to characterize the amplitudes and rates of molecular motions[72]. Typically, experiments are sensitive to slow (milliseconds to seconds), intermediate (microseconds to milliseconds) or fast (picoseconds to microseconds) dynamics. The anisotropic nuclear spin interactions are averaged by intermediate to fast motion. In the simplest case of dipolar couplings, the degree of averaging depends on the geometry of motion of the internuclear vector. The traditional approach for measuring the geometry and rates of motion in these intermediate and fast regimes is through line-shape analysis of 1D ^{2}H or ^{13}C spectra measured as a function of temperature. This typically provides very accurate information about the geometry of motion and can yield precise activation energies[73,74]. However, this approach is limited by low sensitivity and low throughput and requires site-specific isotopic labelling.

A robust and higher-sensitivity approach for measuring the amplitudes of fast motion in systems where selective labelling is not feasible is the 2D dipolar chemical-shift correlation (DIPSHIFT) experiment[75–77] (FIG. 2g). This experiment separates heteronuclear dipolar couplings such as $^{13}C–^{1}H$ and $^{15}N–^{1}H$ by isotropic chemical shifts. Motional averaging of the dipolar couplings is manifested as reduced splitting in the frequency spectra[78–80]. The motional geometry can also be measured using REDOR-recoupled $^{13}C–^{15}N$ dipolar couplings[81,82]. Measurement of motional amplitudes is sensitive to radiofrequency field inhomogeneity and the presence of remote nuclei. To reduce these imperfections, off-MAS experiments, with angle offsets as small as 0.03°, have been proposed[83]. At 100 kHz MAS, variable contact time cross-polarization can be used to measure motionally averaged dipolar couplings[84]. For millisecond-timescale motions, the centreband-only detection of exchange (CODEX) technique[85,86] is a robust approach (FIG. 2h), provided that spin diffusion, which is the relayed transfer

of spin polarization through dipolar coupling, does not occur on the same timescale.

Fast molecular motions can be characterized using NMR relaxation measurements[72]. To determine dynamic models, the longitudinal relaxation rates[87,88] and rotating-frame relaxation rates[89–91] can be measured to probe picosecond to microsecond timescale motions. Here, care has to be taken to avoid spin diffusion, which can average relaxation rates between neighbouring sites, especially when fast-relaxing methyl groups are present[92,93].

High temperature and pressure
Today, high-temperature (above 1,600 K) NMR experiments can be conducted for static samples[94]. For MAS, recent approaches use laser heating, where optical fibres transport the laser to a sample in a ceramic insert within a bottomless rotor[94]. Commercial systems able to heat to ~1,000 K are now available for 7 or 4 mm MAS rotors. For high pressures, progress has been made for static

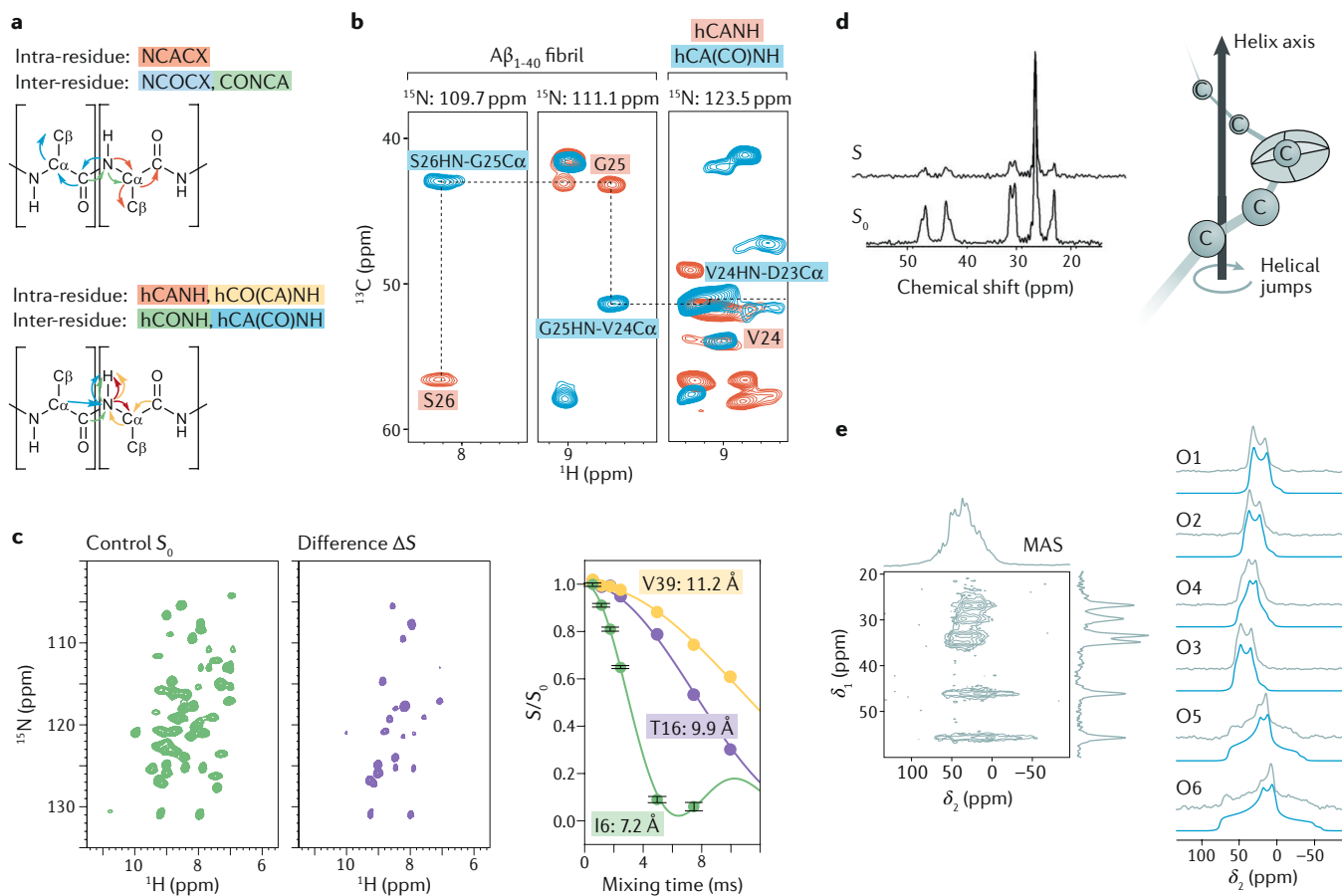Fig. 3 | **Representative solid-state NMR results and experiments.** **a** | Resonance assignment experiments. Chemical shifts of ^{13}C, ^{15}N and ^{1}H are correlated to obtain sequence-specific resonance assignment. **b** | Intra-residue hCANH and inter-residue hCA(CO)NH correlation spectra of Aβ fibrils[318]. **c** | $^{1}H–^{19}F$ rotational echo double resonance (REDOR) spectra for measuring internuclear distances up to 1.5 nm. Spectra shown are for the model protein GB1, where amide protons that are close to the ^{19}F spins manifest intensities in the difference spectrum ΔS[68]. The REDOR dephasing for the cross-peaks is fit to give the $^{1}H–^{19}F$ distances. **d** | Centreband-only detection of exchange (CODEX) spectra of isotactic-poly(4-methyl-1-pentene) to determine the rates of helical jumps of the polymer chain around the helix axis (right)[319]. **e** | ^{17}O magic-angle spinning (MAS) spectra (left) and multiple-quantum MAS (MQMAS, right) spectra of MgSiO$_3$, showing resolution of six distinct oxygen species. Line shapes simulated using density functional theory calculated values are also shown (cyan), enabling assignment of all signals[143]. δ$_1$, chemical shift; NMR, nuclear magnetic resonance; ppm, parts per million; S$_0$, control spectrum; S, dephased spectrum; ΔS, difference spectrum. Part **b** adapted from REF.[318], CC BY 4.0. Part **c** adapted with permission from REF.[68], ACS. Part **d** adapted with permission from REF.[319], RSC. Part **e** adapted with permission from REF.[320], ACS.

samples using diamond anvil cells and Lenz lenses to overcome sensitivity limitations. Experiments up to 90 GPa are now feasible[95]. High-pressure MAS experiments have been performed using sealed rotors and inserts, and a recent design has achieved pressures of 0.04 GPa (REF.[96]).

Dynamic nuclear polarization

The intrinsic nuclear spin polarization in NMR spectroscopy is low because of the relatively small size of the nuclear γ. At magnetic fields of 9.4–18.8 T, the ^{1}H spin polarization is less than 0.007% at ambient temperature. To increase the spin polarization, one approach is to transfer unpaired electron spin polarization to nuclei, as the electron γ is 658-fold greater than the proton γ. Dynamic nuclear polarization (DNP) is the electron to nuclear spin polarization transfer induced by microwave irradiation of the electron paramagnetic resonance. Proposed in the 1950s[97,98], DNP has been successfully integrated into high-field MAS NMR systems since 2008 (REFS[99,100]). The most common microwave source for high-field DNP today is the gyrotron, a microwave oscillator that outputs 10–100 W of power at common NMR frequencies[101]. Gyrotrons are now available up to 593 GHz, corresponding to a ^{1}H Larmor frequency of 900 MHz, with MAS rates up to 65 kHz, thus covering the full range of magnetic fields and MAS frequencies. DNP NMR spectroscopy has fuelled intense research into how to increase the spectral sensitivity of samples from frozen solutions to membrane proteins. In materials research, sensitivity enhancements of two orders of magnitude are now routinely achieved for solid-state NMR spectra of technologically relevant materials[102,103]. Samples are wetted or impregnated with a solution containing a paramagnetic polarization source, such as the biradical AMUPol dissolved in a mixture of D_2O, H_2O and glycerol or dimethylsulfoxide[104], or the hydrophobic biradical TEKPol dissolved in 1,1,2,2-tetrachloroethane[105].

Paramagnetic solid-state NMR

In compounds containing paramagnetic centres such as metalloproteins, inorganic oxides or organometallic compounds, the hyperfine interaction between the unpaired electrons and the nucleus causes large shifts in the NMR frequencies called contact and pseudo-contact shifts[106,107]. This unpaired electron–nucleus interaction also causes paramagnetic relaxation enhancement (PRE) of the nuclear spin in a distance-dependent manner[107,108]. Both effects report the atomic-level structure around the paramagnetic centre. Experiments for measuring pseudo-contact shifts and contact shifts are fundamentally no different from diamagnetic NMR spectroscopy, except for assignment of frequency-shifted resonances. PRE can be measured using regular relaxation NMR experiments after comparison with the relaxation rates of a diamagnetic sample. Paramagnetic ions such as Mn^{2+} and Cu^{2+} can be incorporated into samples as free ions[109,110], part of a chemical tag[111,112] or a metalloprotein complex[113] to serve as distance probes. In addition, paramagnetic doping combined with fast MAS speeds up data acquisition

by one or two orders of magnitude by reducing nuclear spin relaxation times[114].

Results

Assignment of multidimensional spectra

Chemical shift assignment is a prerequisite for extracting structural and dynamic information from NMR spectra. Small molecules and natural abundance compounds can often be assigned from 1D spectra based on characteristic chemical shifts alone. To simplify these 1D spectra, experiments that selectively detect CH, CH_2 or CH_3 groups (sometimes called spectral editing experiments) are often used to aid assignment[115–117]. For proteins and other biopolymers, the large number of peaks can usually only be resolved and assigned in multidimensional correlation spectra. This assignment is based on connecting peaks that share a common chemical shift in a particular dimension of a 2D or 3D spectrum. For example, a Cα–Cβ correlation peak and a Cγ–Cβ peak in a 2D ^{13}C–^{13}C spectrum will manifest the same Cβ chemical shift in the F2 dimension of the spectrum. For proteins, the NCACX spectrum correlates nitrogen, Cα and CO chemical shifts within the same residue, whereas the NCOCX spectrum correlates the nitrogen chemical shift of a residue with the CO and Cα chemical shifts of the preceding residue[118–120] (FIG. 3a). For ^{1}H-detected 2D and 3D experiments such as the hNH experiment (FIG. 2i), the ^{1}H and ^{15}N chemical shifts serve as the read-out of the Cα and CO chemical shifts of two sequential residues[19]. A representative strip of ^{1}H-detected 3D spectra of the Alzheimer disease Aβ peptide is shown in FIG. 3b.

Distance measurements

Qualitative distance restraints can be extracted from 2D and 3D correlation spectra based on the shortest mixing times at which a peak appears. These restraints are typically reported as upper bounds, because peak intensities also depend on experimental conditions: cross-peak intensities generally decrease with increasing B_0, MAS rate and spin diffusion mixing times. The upper-bound distance is usually calibrated using model compounds with known distances. For uniformly ^{13}C-labelled proteins, on an 800 MHz spectrometer under 10 kHz MAS, cross-peaks that appear after 100 ms, 250 ms and 500 ms spin diffusion have been estimated to correspond to ^{13}C–^{13}C distance upper limits of 6.0 Å, 7.0 Å and 8.0 Å, respectively[55]. Longer ^{13}C–^{13}C distances can be probed qualitatively using ^{1}H-mediated recoupling experiments such as phase-alternated rotation of magnetization and pulsed proton-assisted recoupling[121,122]. More quantitative ^{13}C–^{13}C distances can be measured using recoupling techniques such as finite-pulse radiofrequency-driven recoupling[123].

Quantitative heteronuclear distances can be extracted from REDOR dipolar dephasing as a function of mixing time (FIG. 3c). The shape of the REDOR dephasing curve is invariant to the product of the dipolar coupling strength and mixing time. Thus, short and long distances have the same universal curve[59], which significantly facilitates distance analysis. Even at fast MAS rates of ~40 kHz, where the 180° pulses occupy a sizeable fraction of the rotor period, REDOR dephasing is still

---

Paramagnetic
Weakly attracted by an externally applied magnetic field, typically as a result of the presence of unpaired electrons.

relatively quantitative, and the finite pulse-length effect can be treated analytically[124]. When the spins have large CSAs and the 180° pulses cause incomplete inversion, the imperfection can be accounted for in numerical simulations. This approach has been used to analyse ^{13}C–^{19}F REDOR data at moderately high magnetic fields where the ^{19}F CSA is large[67].

Long distances to ~2 nm can also be measured semiquantitatively using paramagnetic relaxation enhancement NMR spectroscopy. ^{15}N and ^1H relaxation experiments on Cu^{2+} and Gd^{3+}-tagged proteins have been used to measure solvent accessibility to proteins[112], Cu^{2+} binding sites in influenza M2 (REF.[125]), $A\beta_{40}$ fibrils[110] and human prion protein fibrils[126]. Paramagnetic Mn^{2+} introduced to lipid bilayer surfaces has been used to measure the depth of insertion of membrane protein in lipid bilayers[109,127].

Motional amplitudes and rates

Measurement of motionally averaged couplings and nuclear spin relaxation rates provides rich information about motional geometry and rates. For characterizing motional amplitudes, the DIPSHIFT class of experiments has been used extensively to obtain order parameters in membrane-bound helical bundles[128,129], dynamically disordered polymers in biomaterials[130] and functionally important side-chain motions in ion channels[131]. Longitudinal, rotating-frame, cross-relaxation rates and order parameters can be analysed using a so-called extended model-free formalism, which yields correlation times for fast and slow internal motions of the protein[89,132,133]. In the absence of overall tumbling, these relaxation data have allowed the studies of protein rocking motions in crystals[134,135]. Temperature-dependent NMR relaxation data provide information about the energetics of molecular motion and have been used to demonstrate coupling between protein dynamics and solvent dynamics[136]. Relaxation data can also be analysed in conjunction with molecular dynamics simulations to quantify motion, as shown for heterokaryon incompatibility protein (HET) amyloid fibrils[137]. Microsecond to millisecond peptide backbone dynamics can be observed through ^{15}N rotating-frame relaxation dispersion experiments[89], as shown for a variant of the human prion protein, Y145Stop[138]. Finally, ^1H-detected fast MAS experiments combined with tailored isotopic labelling have allowed high-resolution characterization of the amplitudes and rates of phenylalanine ring flips in the large (~0.5 MDa) enzyme complex dodecameric aminopeptidase TET2 (REF.[139]).

In semi-crystalline polymers, the mobility of polymer chains in the crystalline region is directly related to the bulk mechanical properties of the materials. For example, poly(4-methyl-1-pentene) (P4M1P) has a helical 7_2 structure in crystallites in which chain defects travel by discrete rotation and translation around the helical axis that reproduce the original structure. The jump angles and activation energies can be determined quantitatively by NMR spectroscopy using CODEX experiments[85] (FIG. 3d). These experiments revealed jump angles of ~103° and jump rates with correlation times between 10 s and 15 ms at 305 K and 360 K, respectively.

Quadrupolar NMR spectra of solids

The NMR spectra of quadrupolar nuclei display broad line shapes and spinning sideband manifolds owing to the large anisotropy[29,30,140]. Fitting programs that minimize the difference between simulated and experimental spectra can be used to extract the magnitude and asymmetry of the quadrupolar tensor[141,142]. If a spin is affected by more than one interaction, the line shape will also depend on the relative orientation of the interaction tensors. In some cases, the NMR parameters can be directly related to structure, whereas in others chemical information is obtained by comparison with similar materials or with NMR parameters predicted by first-principles calculations. The different dependence of the quadrupolar interaction and CSA on the magnetic field means that multi-field measurements are vital to structural analysis[33].

MQMAS experiments resolve the signals of all species in the sample and the individual line shapes of each species, as shown in FIG. 3e for ^{17}O NMR spectroscopy of a silicate mineral[143–146]. The relative amounts of each species have to be corrected for the different excitation efficiencies by comparison with numerical simulations. From each MAS line shape, the magnitude and asymmetry of the quadrupolar interaction and isotropic chemical shift can be extracted and used as starting points for multi-parameter fits of the complete spectrum. The position of the spectral line shape in an MQMAS spectrum provides an alternative source of information on the quadrupolar and chemical shift parameters. For disordered materials such as glasses, information about structural distributions can be obtained from MAS or MQMAS spectra[146]. As the magnitude and asymmetry are both related to the principal components of the quadrupolar tensor, it is often assumed that a joint distribution of these parameters can be described using the Czjzek model[147]. This is an area where isotropic–anisotropic correlation approaches such as dynamic-angle spinning[28] can also be highly informative and have been used to extract correlations between quadrupolar parameters in densified silica glasses to gain insight into bond-length and bond-angle distributions[148].

Computation of NMR parameters

Computational methods are increasingly used to support interpreting, assigning and predicting the solid-state NMR spectra of materials[149,150]. Density functional theory (DFT) is the method of choice, owing to its balance of efficiency and accuracy, with many studies carried out using periodic plane-wave codes[151] to exploit the inherent translational symmetry of solids. Calculations determine the electronic structure for a particular arrangement of atoms, and from this the shielding, quadrupolar and J coupling tensors for any nucleus can be calculated. In the simplest cases, NMR parameters are predicted from structural models obtained from diffraction and matched to the experimental data. Calculations allow the assignment of signals in NMR spectra to specific sites (FIG. 3e) and can help identify overlapped or missing signals. The joint use of NMR spectroscopy and computation for structural analysis is often referred to as NMR crystallography[149,150].

Molecular dynamics
A computer-simulation method for characterizing the dynamics of atoms and molecules, providing an overview of how they move over a period of time.

Density functional theory
(DFT). A computational quantum-mechanical modelling approach used to investigate electronic structure in many-body systems.

If less is known about the atomic structure of the solid, generating structural models is more challenging. When partial structures are available, possible structural models can be produced using automated algorithms, structure searching approaches or Monte Carlo methods, as demonstrated on proteins, ceramics, microporous materials, pharmaceuticals and glasses[150]. Comparison of predicted and experimental parameters can then be used to refine the atomic coordinates[152]. When no prior information is available, powder crystallography of molecular solids involves the combination of de novo structure prediction, DFT calculation and measured chemical shifts[153].

For disordered materials, calculations of manually modified models of ordered analogues predict the magnitude and direction of changes in the quadrupolar and/or shielding NMR parameters. These changes include variations in the type of atoms present (compositional disorder) or variations of the exact atomic arrangements (positional disorder). Multiple models can then be compared in terms of their energies and agreement with the measured NMR parameters[149,154]. For amorphous materials such as glasses, the most successful approaches exploit molecular dynamics simulations, with initial configurations generated using a random distribution of the specified number of atoms[155].

Applications
Protein structural biology
X-ray crystallography and cryo-electron microscopy can both provide atomic structures of large proteins and protein complexes. However, dynamically disordered or heterogeneous systems are not easily amenable to these approaches. As a result, membrane proteins that contain small soluble domains, polymorphic amyloid fibrils or polydisperse protein complexes that are conformationally plastic are uniquely suited to solid-state NMR analyses.

Membrane proteins. Multidimensional correlation ^{13}C, ^{15}N and ^{1}H NMR spectroscopy has been applied to many membrane proteins to elucidate their structure, dynamics and mechanism of action. These membrane proteins include proton channels[128,156,157], potassium channels[158–160], transporters[161,162], seven-transmembrane helix proteins[163,164], β-barrel proteins[165] and antibiotic membrane peptides[166]. Assignment of ^{13}C and ^{15}N chemical shifts provides the first line of information about backbone conformation. Chemical shifts reveal the positions of disordered segments in predominantly α-helical membrane proteins[128] and report protein conformational changes[167]. Chemical shift changes have been used to detect pH-induced conformational changes of the influenza M2 protein[168] (FIG. 4a), coupled structural changes between the pH gate and selectivity filter of potassium channels[167], conformational changes of an ABC transporter upon binding to nucleotides[169] and light-induced conformational changes of subunit interfaces in proteorhodopsin[170] (FIG. 4b). To detect conformational changes of large membrane proteins, pairwise amino acid labelling combined with DNP is an effective approach[171]. With sensitivity enhancement, protonation

and structural changes of key residues in bacteriorhodopsin are observed that reveal the proton transfer mechanism of this light-induced ion pump[172]. ^{1}H-detected NMR experiments have enabled high-resolution characterization of β-barrel membrane proteins[165]. ^{15}N longitudinal and rotating-frame relaxation experiments have been used to measure the amplitudes and rates of slow motions in the seven-transmembrane helix protein sensory rhodopsin[173]. Finally, studies of water interactions with membrane proteins have given insights into the mechanism of ion conduction by channel proteins[160].

Ligand binding and dynamics are critical to the function of many membrane proteins. ^{19}F NMR spectroscopy is well suited to measure ligand-binding sites in proteins, by orthogonal labelling of the ligand and the protein. Fluorinated cholesterol has been used to identify the cholesterol-binding site in influenza M2 (REF.[64]). This binding is important for M2-mediated virus budding and membrane scission. Mixed fluorinated and ^{13}C-labelled proteins have been used to determine the tetrameric structure of the influenza B M2 protein[128].

Amyloid proteins. Solid-state NMR spectroscopy is well suited to the characterization of amyloid proteins[174], many of which form as a result of protein misfolding in diseases. These proteins form extended cross-β fibrils with high 1D order, which gives rise to well-resolved NMR spectra. Recent examples of NMR-characterized amyloid proteins include Alzheimer's disease Aβ peptide[175–177], α-synuclein[178,179], transthyretin[180], β$_2$-microglobulin[181], fused in sarcoma (FUS)[182], tau[183] and immunoglobulin light chains[184,185]. In addition to the fibril structure, solid-state NMR spectroscopy has been used to investigate small-molecule binding to these fibrils. For example, the binding of sulindac sulfide, a non-steroidal anti-inflammatory drug, to Aβ$_{40}$ fibrils was studied using REDOR experiments[186] (FIG. 4c). Epigallocatechin gallate, a compound found in green tea, binds Aβ$_{40}$ monomers to induce the formation of non-toxic spherical aggregates[187]. Amyloid intermediates and oligomers, which are too dynamically disordered to be studied by cryo-electron microscopy, have been studied by observing the chemical shift distribution in NMR spectra[188]. The data indicate the presence of significant β-strand segments before the formation of mature fibrils. The interactions of Aβ, α-synuclein and human islet amyloid protein with lipid membranes have been studied to understand the mechanisms of neurotoxicity and fibril transmission between cells[189,190]. Finally, measurement of the interactions of amyloid proteins with water[191–193] provides insight into the stability and water-accessibility of these fibrils.

Whereas many amyloid proteins are involved in disease, other amyloid proteins carry out biological function and occur during pharmaceutical formulation. For example, the Het-S protein of filamentous fungi forms a β-solenoid structure[194]. Amyloid fibrils formed by the peptide hormones glucagon[195] and β-endorphin[196] have been structurally characterized. Whereas most amyloid fibrils exhibit parallel in-register β-strand structures, glucagon forms a novel antiparallel hydrogen-bonded β-sheet structure containing two coexisting molecular

---

Cryo-electron microscopy
A technique used to determine the 3D structure of samples frozen at cryogenic temperatures, which are not in a crystalline form.

conformations[195] (FIG. 4d). This result showcases the structural diversity of amyloid proteins and suggests approaches to design fibrillization-resistant glucagon analogues to improve the solution stability of this anti-hypoglycaemia drug.

Protein complexes. Solid-state NMR spectroscopy is increasingly applied to heterogeneous and dynamic protein complexes. These complexes can be sedimented from solution into MAS rotors or directly spun into the rotor to collect the solid[197]. This sedimentation NMR
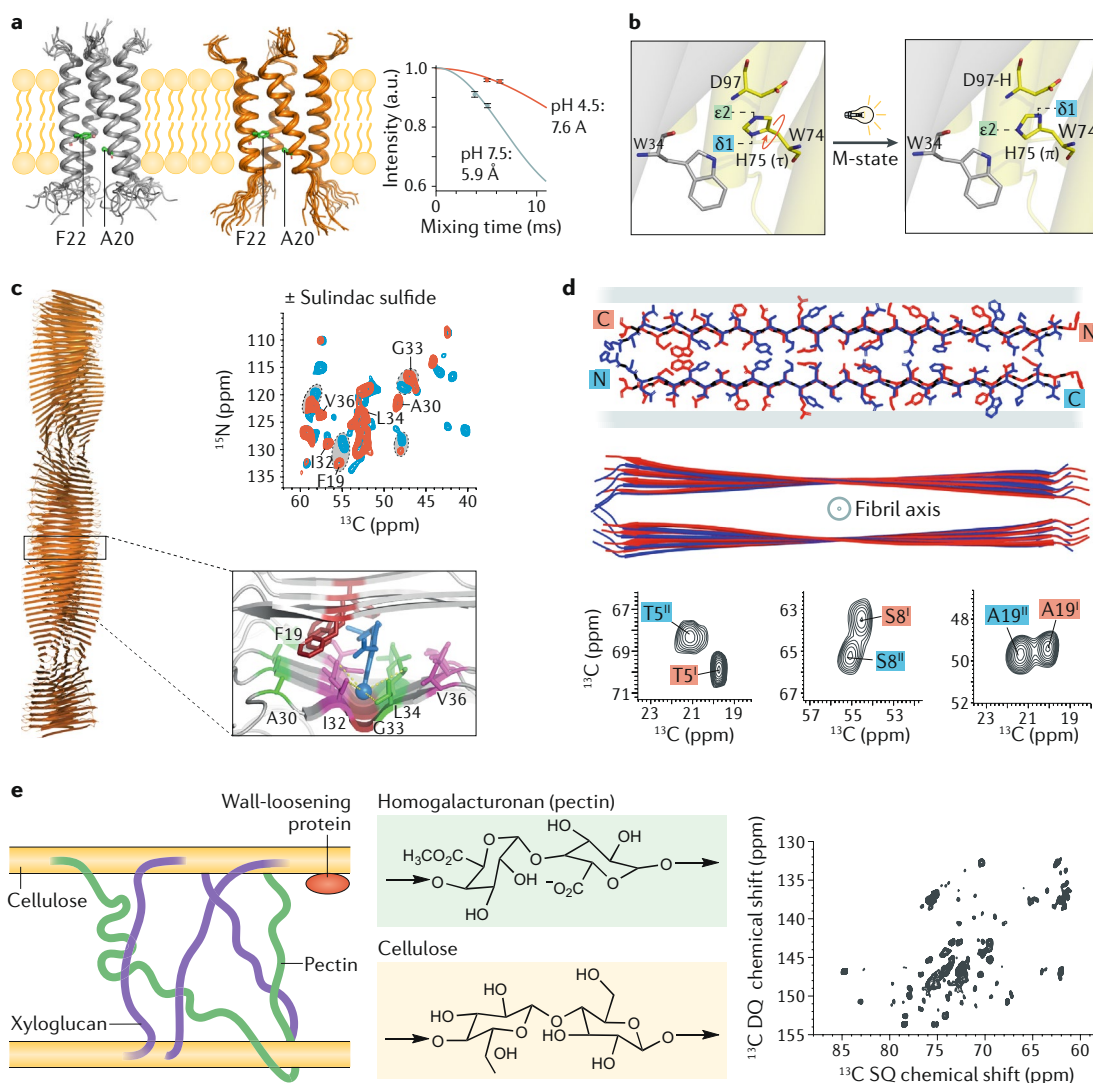

Fig. 4 | **Applications of solid-state NMR spectroscopy to biological chemistry. a,b** | Examples of membrane protein studies. **a** | Atomic-resolution structures of the influenza B M2 proton channel in its closed and open states[128]. The structures, determined using interhelical distance experiments such as ^{13}C–^{19}F rotational echo double resonance (REDOR) and orientation experiments, reveal a distinct activation mechanism of the channel compared with the influenza A M2 protein. **b** | Structural changes of an Asp-His-Trp triad in the pentameric light-driven proton pump, green proteorhodopsin (GPR)[170]. Dynamic nuclear polarization (DNP) nuclear magnetic resonance (NMR) experiments revealed tautomeric and rotameric structural changes of His75 to mediate proton transfer. **c,d** | Examples of amyloid fibril studies. **c** | The binding site of sulindac sulfide to the Alzheimer disease Aβ peptide is determined by 2D correlation NMR experiments and chemical shift perturbation[186]. Structure on the left was generated using the Protein Data Bank: 2LMN[324]. **d** | Atomic-resolution structure of the glucagon amyloid fibril. The peptide assembles as an antiparallel cross-β fibril that contains two coexisting molecular conformations. These two conformations are manifested as two sets of chemical shifts for each atom in the spectra[195]. **e** | The polysaccharide-rich cell walls of plants, bacteria and fungi can be studied using 2D and 3D NMR to understand how macromolecular packing and dynamics explain the properties of these biomaterials. The 2D ^{13}C refocused incredible natural abundance double quantum transfer experiment (INADEQUATE) correlation spectra[210] resolve the chemical shifts of dynamic matrix polysaccharides in *Arabidopsis* cell walls. DQ, double quantum; ppm, parts per million; SQ, single quantum. Part **a** adapted from REF.[128], Springer Nature Limited. Part **b** adapted with permission from REF.[170], PNAS. Part **c**, this research was originally published in the *Journal of Biological Chemistry*. Prade, E. et al. Structural mechanism of the interaction of Alzheimer disease Aβ fibrils with the non-steroidal anti-inflammatory drug (NSAID) sulindac sulfide. *J. Biol. Chem.* 2015; **290**, 28737–28745, REF.[186]. © the American Society for Biochemistry and Molecular Biology. Part **d** adapted from REF.[195], Springer Nature Limited. Part **e** adapted with permission from REF.[210], Oxford University Press.

approach, together with other methods, has been used to characterize microtubule-bound motor proteins[198], the HIV capsid protein[199], the 20S proteasome[200], the 50S ribosome[201] and protein–protein interactions between GB1 and immunoglobulin[112]. These studies have given insights into the structural stability and activation of these assemblies. For example, αB crystallin, which assembles into a polydisperse and dynamic complex, was found to interact with amorphous client proteins and fibril-forming proteins at different interfaces[202]. ¹H-detected NMR experiments on the 14-subunit complex of caseinolytic protease[203] revealed the binding site of an inhibitor, bortezomib. Site-specific measurement of the motional amplitudes of the HIV capsid protein revealed the flexibility of a loop domain and its rigidification upon binding to a host protein, cyclophilin A[199]. For metalloproteins such as superoxide dismutase and matrix metalloproteinase 12 (MMP12), pseudo-contact shifts and paramagnetic relaxation enhancement measurements[204,205] allowed structure determination. Other dynamic assemblies involving hydrogels and phase-separated biomolecules such as membraneless cellular organelles are also being investigated[206]. Fast MAS is instrumental for studying these paramagnetic proteins, by averaging the dipolar coupling contribution to the resonance linewidth, especially near the paramagnetic centre, thus revealing the structure of the metal coordination sphere with high precision[207].

Cell walls and extracellular matrices

The glycan-rich matrix on the cell surfaces of plants, bacteria and fungi is well suited to solid-state NMR studies. Cell walls and extracellular matrices contain carbohydrates, proteins, lignin and other biopolymers. These biomaterials can be investigated using ¹³C, ¹⁵N and ¹H NMR experiments[208]. Both isotopically enriched and natural abundance samples can be studied, the latter often requiring DNP[209]. For plants, the primary cell walls of both dicots and monocots have been extensively studied using ¹³C NMR spectroscopy[210] (FIG. 4e). The refocused INADEQUATE experiment is particularly effective for identifying dynamic polysaccharides such as homogalacturonan. 3D ¹³C correlation NMR experiments further resolve the signals[211] and enable the detection of intermolecular contacts. These data have revised the conventional model of primary cell wall structures, indicating that cellulose, hemicellulose and pectins exist in a single network rather than two separate networks. High-field 2D ¹³C MAS NMR spectra resolved multiple conformations of cellulose[212] and xylan[213] and distinguished the conformation of the chemically reactive hydroxymethyl groups in cellulose[214]. DNP-enhanced NMR spectroscopy has been used to determine the site of protein binding to cellulose microfibrils to loosen the cell wall for plant growth[215]. DNP experiments have also been used to investigate lignin interaction with xylan and cellulose in plant secondary cell walls[216]. 2D ¹³C NMR spectroscopy has been applied to fungal cell walls to show a layered structure composed of chitin and diverse glucans[217]. For bacterial cell walls, DNP[209] and ¹H-detected NMR experiments[218] have been used to study peptidoglycan structure. Finally, the bacterial extracellular matrix has been studied using quantitative ¹³C NMR spectroscopy to determine the composition of polysaccharides and proteins[219] and to discover a new form of cellulose, covalently linked to phosphoethanolamine, in *Escherichia coli* biofilm[220].

Organic and molecular solids

One of the main applications of solid-state NMR spectroscopy is the characterization of powdered molecular solids. Chemical shifts can be readily measured and compared with those of known compounds or calculated shifts to test structural hypotheses. ¹³C and ¹H chemical shifts can be measured from 1D ¹³C CPMAS, 2D ¹H–¹³C HETCOR or ¹H fast MAS spectra. They can be assigned with 2D ¹H–¹³C HETCOR or ¹³C INADEQUATE spectra enhanced with DNP[221]. This approach has been widely applied to crystalline polymorphs of pharmaceutical compounds[23,222,223]. For example, it was used to elucidate the stabilization mechanism of an amorphous form of tenapanor hydrochloride[224]. More sophisticated approaches for de novo structure determination combine computational structure prediction with experimental chemical shifts or distance restraints. This has led to complete 3D structures of microcrystalline drugs and organic CO_2 capture materials[225,226]. These structures can be quantified in terms of probability and precision[227], with average displacement parameters of 0.01 Å² for a recent structure of ampicillin[226]. Using fast MAS and DNP NMR spectroscopy, sensitivity is now sufficient to characterize pharmaceutical polymorphs in situ, as embedded in formulations[102,228]. These methods can be used to identify interactions between the different components of the formulation, leading to better understanding of drug release. Because solid-state NMR spectroscopy does not require long-range order to produce high-resolution spectra, characterizing mixtures and observing impurities are straightforward. With sensitivity enhancements by DNP, the detection limit for MAS NMR spectroscopy has improved to ~80 pmol. For example, the ³¹P signal of a single phosphodiester in DNA oligomers attached to a glass plate has been observed[229].

To characterize supramolecular systems, high-resolution ¹H spectra have allowed the measurement of interatomic distances, often to hydrogen-bonded protons. This approach has been used, for example, to study the structures of self-assembled G quartets[230] or to reveal intermolecular hydrogen-bonding and dynamics in a deep eutectic pharmaceutical[231]. Molecular mobility plays an important role in the properties of these supramolecular systems. In addition to ²H NMR line shapes, isotropic and anisotropic chemical shifts have been employed to study dynamic processes such as thermally activated rotational dynamics of hydrogen-bonded and charge-transferred diazabicyclo[2.2.2]octane molecular rotors[232].

Domain structures in molecular solids can be characterized using spin diffusion NMR spectroscopy[233]. Spin diffusion of DNP-hyperpolarized magnetization has been used to characterize API distributions within lipid nanoparticles[234] and to identify core-shell structures in organic crystalline nanoparticles[235].

Solid-state NMR spectroscopy is currently the best available method for quantitative characterization of the chemical composition of complex organic materials and other carbon-rich materials. Relative peak areas in multi-cross-polarization spectra[236] or fully relaxed direct-polarization NMR spectra provide the relative concentrations of functional groups, unlike in Raman and infrared spectroscopies. In carbon X-ray photoelectron spectroscopy, the number of resolved peaks is usually ten times smaller than in NMR spectra that selectively detect the signals of quaternary carbons, CH, CH₂, sp^3-hybridized carbon and N-bonded carbon[237]. Solid-state NMR spectroscopy can quantitatively determine functional groups and aromaticity in carbon materials such as char residues[238], whereas the aromatic cluster size can be estimated based on recoupled dipolar dephasing. In addition, using dipolar couplings and spin diffusion, one can determine the proximity between different components and domain thicknesses on a scale of 1–40 nm, for instance in complex materials such as polymer–molecular organic framework (MOF) composites[239] or the organic–inorganic nanocomposite in bone[240,241].

Inorganic and hybrid materials

Solid-state NMR spectroscopy is a key tool for the structural characterization of oxides, whose chemical flexibility allows tuning of physical and chemical properties for a wide range of applications such as electronics, ceramics, energy materials and catalysis (FIG. 5)[146]. Compositional disorder is often studied by combining NMR spectroscopy and DFT calculations, as described above, with recent applications to pyrochlores[242], fluorites[243] and oxide catalysts[244–246]. Hybrid perovskite structures have recently been the subject of intense NMR studies to determine the composition, phase segregation or layer structures in 2D materials[247–249]. Variable temperature measurements are used to study the dynamics in oxides such as ZrW_2O_8 (REF.[250]), where 2D exchange NMR spectroscopy was used to show that negative thermal expansion resulted from a 'ratchet-like' mechanism in which all oxygen species interconvert. The sensitivity of solid-state NMR spectroscopy to dynamics has also allowed extensive studies of lithium ion batteries[146,251,252]. In situ and in operando $^6Li/^7Li$, ^{31}P, ^{17}O and ^{23}Na NMR experiments[251] have used plastic cell capsules to create a working device, allowing the determination of the phases formed as batteries are cycled, and tracking dendrite formation and battery failure[251]. Recently, the study of oxides has been extended to nanoparticles and the importance of the surface chemistry in processes such as catalysis[253].

Solid-state NMR spectroscopy has found considerable application in the study of silicate minerals and clays, with ^{29}Si chemical shifts sensitive to the number and type of coordinating atoms, next-nearest neighbouring nuclei and chain polymerization[146,254,255]. Multinuclear NMR studies have explored cation and anion disorder[256,257], the substitution of paramagnetic impurities[146,258] and radiation damage in natural minerals[146]. For mantle minerals[255], the high pressure required for synthesis using multi-anvil presses limits the sample volume. Thus, approaches to improve sensitivity

such as composite pulses, where multiple pulses are used in place of a single pulse to increase efficiency[29], satellite-transition MAS[259,260] and isotopic enrichment[12,261] are required. Computation augments these experiments, as shown in recent work on the hydration of deep Earth silicates using random structure searching and ^1H, ^{29}Si and ^{17}O NMR spectroscopy[261,262] (FIG. 5a).

Microporous and mesoporous materials, including zeolites, phosphate-based organic frameworks and MOFs (FIG. 5b,c), are important in gas storage, drug delivery and catalysis[146,263]. The combination of compositional, positional and dynamic disorder in these systems makes NMR ideal for studying their structure and reactivity. Solid-state NMR spectroscopy is widely used to understand the number, distribution and strength of acid sites in zeolites[146] using probe molecules. Recent work has exploited ^{17}O enrichment to demonstrate the unexpected lability of the framework bonds[264]. In situ experiments have been used to probe the reactivity and hydrolytic disassembly of zeolites[146,265]. For aluminophosphates, ^{27}Al MAS and MQMAS and $^{27}Al/^{31}P$ heteronuclear multiple quantum coherence experiments have been combined with DFT calculations to study cation disorder, anion disorder and dynamics of guest molecules within the pores[146,266,267]. The chemical flexibility of MOFs allows fine-tuning of the pore size and chemical properties[268,269], and NMR can be used to study the nodes, organic linkers and guest molecules. Recent work on mixed-linker MOFs[270] used $^{13}C-^{15}N$ REDOR experiments to measure internuclear distances. Comparison with molecular dynamics calculations showed that alternation of the three different linkers was present. The binding of guest molecules to open metal sites (particularly CO_2) has also been studied using NMR spectroscopy[269].

Disordered and amorphous materials such as ceramics (FIG. 5d), glasses (FIG. 5e) and cements, as well as the chemically and structurally heterogeneous inorganic–organic hybrid materials[271], pose considerable challenges for structural analysis, and NMR spectroscopy is the method of choice for studying these materials. The distribution of structural environments leads to a range of NMR parameters and overlapped spectral line shapes[146,272]. The relation between NMR parameters and local geometry has also been probed by molecular dynamics simulations[155] that generate a suite of possible structures for which DFT calculations can predict the NMR parameters. Recent ^{89}Y NMR spectroscopy of oxide ceramics[242] used an ensemble-based modelling approach, considering every possible arrangement of atoms, and simulated the NMR spectra to compare with the experiment. For cements, ^1H, ^{27}Al and ^{29}Si NMR experiments are widely used to probe local structure, and ^{43}Ca NMR spectroscopy is becoming increasingly more viable as magnetic field strengths increase, overcoming the dual challenges of low γ and quadrupolar broadening. Detailed atomic-level information on the role of water and retardants such as sucrose were obtained using 2D correlation NMR experiments[273]. DNP has enabled the measurement of correlations between silicon atoms and between silicon and aluminium atoms with high sensitivity. By combining these results with
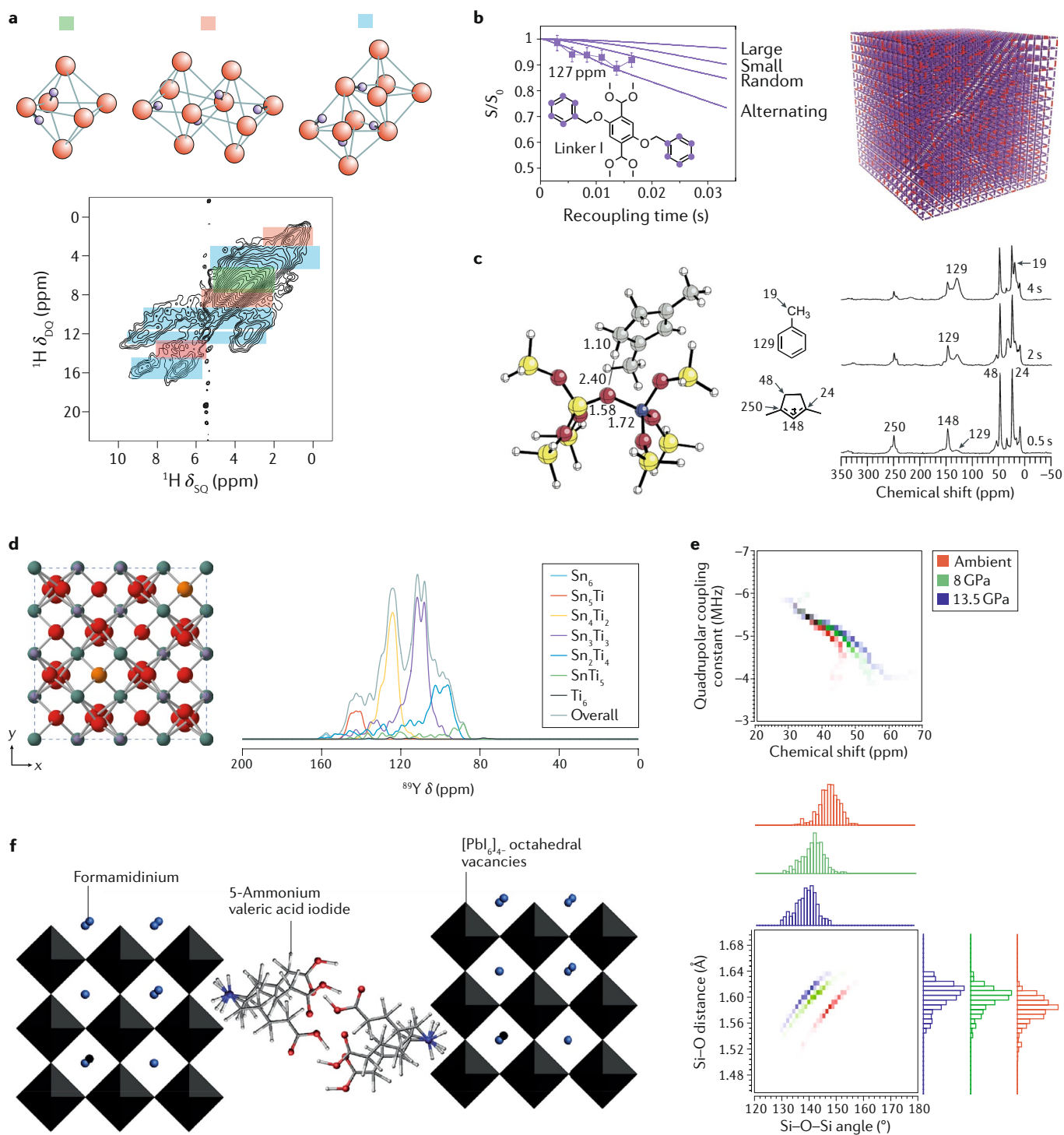
simulations and DFT chemical shift calculations, the full 3D atomic structures of cementitious calcium silicate hydrate and calcium aluminate silicate hydrate can be determined[274]. Also, hybrid materials containing calcium phosphate have been of interest, owing to the role they play in biomaterials such as bone, bioglasses and synthetic apatites. Whereas most studies exploit ^1H, ^{13}C and ^{31}P NMR spectroscopy, ^{43}Ca and ^{17}O NMR experiments are becoming increasingly used[241]. Recent work performing ex vivo microimaging of an intact mouse tooth under MAS was able to selectively identify and

locate the mineral and organic components with high spatial resolution ($\sim$100 μm)[275].

For inorganic semiconductor and metal nanoparticles, ^{13}C and ^{31}P NMR spectroscopy give detailed information on the composition of the organic capping groups on the surface of nanoparticles that govern their size and shape[276]. Solid-state ^{77}Se, ^{31}P, ^{113}Cd or ^{119}Sn NMR experiments of InP, GaP, CdSe, CdS and SnO_2 nanoparticles show clear differences between the surface and bulk. The reactivity of metal nanoparticles has been widely studied using surface probe molecules to understand the

Fig. 5 | **Applications of solid-state NMR spectroscopy to materials chemistry.**
a | Prediction of the hydrous defects in wadsleyite, an inner Earth mineral found at depths of 400–600 km. Structure searching is used to predict possible structures for which nuclear magnetic resonance (NMR) parameters are calculated using density functional theory (DFT). Shaded boxes in spectra represent where structures (colours coordinate) were predicted[261]. **b** | Determination of the mesoscale structure of multivariate molecular organic frameworks containing linkers with different functional groups[270]. ^{13}C–^{15}N rotational echo double resonance (REDOR) combined with molecular dynamics simulations allow the distinction of alternating cluster forms from random, small and large cluster forms. **c** | ^{13}C cross-polarization magic-angle spinning (CPMAS) spectra of high-temperature reaction products of ethylene–$^{13}C2$ on zeolite HZSM-5 catalyst beds[321]. The spectra elucidated the mechanism of methanol to hydrocarbon catalysis, establishing that methanol and dimethyl ether react on cyclic organic species contained in the cages or channels of the inorganic host. **d** | Prediction of ^{89}Y NMR spectra of pyrochlores using ensemble-based modelling. NMR parameters of all possible cation arrangements are predicted using DFT and their Boltzmann-weighted contributions to the spectrum are then determined to obtain detailed information on the local geometry[242]. **e** | Pressure-induced evolution of the distributions of the Si–O distances and Si–O–Si inter-tetrahedral bond angles in vitreous silica quenched from high pressure. 2D dynamic angle-spinning ^{17}O NMR spectra show that, with increasing pressure, the mean Si–O–Si bond angle decreases whereas the mean Si–O distance increases[148]. **f** | Structure of inorganic–organic hybrid perovskites[322]. 5-Ammonium valeric acid iodide was used to stabilize the structure of α-FAPbI3. MAS NMR spectroscopy in combination with DFT was used to determine the atomic-level structure. DQ, double quantum; ppm, parts per million; SQ, single quantum. Part **a** adapted from REF.[261], CC BY 4.0. Part **b** adapted with permission from REF.[270], AAAS. Part **c** adapted with permission from REF.[321], ACS. Part **d** adapted with permission from REF.[242], ACS (https://pubs.acs.org/doi/10.1021/jacs.9b09036); further permissions related to the material excerpted should be directed to the ACS. Part **e** adapted with permission from REF.[148], AIP. Part **f** adapted with permission from REF.[322], ACS.

state of metal atoms at surfaces. Gold nanoparticles have been extensively studied, leading to the determination of the complete structures of surface capping groups[277]. Also, the mode of ligands binding to the surface of nanoparticles has been determined using 2D NMR spectroscopy. In CdSe nanoparticles, detailed analysis of the interactions between hexadecylamine and thiophenol capping ligands and the surface cadmium and selenium atoms using ^{1}H–^{113}Cd and ^{1}H–^{77}Se CPMAS HETCOR indicated that thiophenol binds to nanoparticles by occupying a selenium vacancy site[278].

Some of the most interesting features of materials occur on surfaces or at interfaces, which have traditionally been studied by cross-polarization experiments to exploit the presence of protons only on the surface of a material. For example, ^{1}H NMR experiments in combination with extended X-ray absorption fine structure measurements revealed the dissociation mechanism of N_2 on tantalum surface sites supported on silica surfaces[279]. ^{1}H–^{13}C and ^{1}H–^{29}Si HETCOR experiments were also used under fast MAS to provide insight into the conformation of allyl groups covalently anchored to the surface of MCM-41 silica surfaces[280]. ^{17}O NMR experiments in combination with surface selective isotopic labelling were used to show that ^{17}O resonances arising from the first to third surface layers, hydroxyl sites and oxygen atoms near vacancies can be distinguished from the bulk[281]. However, low sensitivity has severely restricted such applications. The introduction of DNP surface-enhanced NMR spectroscopy has largely solved this problem in the past decade[103]. DNP surface-enhanced NMR spectroscopy has been deployed to determine the structures of organometallic ligands on surfaces[282] and the Brønsted acidity of surface hydroxyls in silica and silica–alumina materials[283,284].

Extended X-ray absorption fine structure
An X-ray absorption spectroscopy technique that is amenable for non-uniform crystalline samples.

Overall utility of solid-state NMR
In summary, for biological chemistry, solid-state NMR spectroscopy is well equipped to elucidate small-molecule binding to biomacromolecules, functionally important protein and ligand dynamics, and chemical processes such as protonation reactions. These applications are highly complementary to X-ray and cryo-electron microscopy approaches. For materials chemistry, the sensitivity of NMR spectroscopy to the atomic-scale environment allows elucidation of the types and levels of static and dynamic disorder, which are vital to understanding chemical reactivity.

Reproducibility and data deposition
Reproducibility of solid-state NMR data
Solid-state NMR spectra are largely reproducible because they are averaged over multiple acquisitions and reflect ensemble averages of nuclear spin properties. Thus, if the same experiment is run with the same acquisition parameters, on the same sample and using the same NMR probe, then spectra should be reproducible to within their signal-to-noise ratio. However, differences in sample preparation can cause variations in NMR spectra, as chemical shifts reflect the environment around each nucleus and are thus sensitive to conformational heterogeneity. Second, phase transients and radiofrequency inhomogeneity vary between probes, which influence pulse sequence performance[285]. This probe-specific variation can affect the reproducibility of spectral intensities. Similarly, experiments that require a precise choice of radiofrequency fields, such as the proton-assisted insensitive nuclei cross-polarization experiment, may make it difficult to obtain reproducible spectral intensities[286]. To achieve high spectral reproducibility, it is thus important to report the full sample preparation conditions and experimental acquisition and processing parameters when publishing experimental data.

Deposition of solid-state NMR data
It is recommended that all raw NMR data associated with publications are deposited for open access. This is a rapidly evolving area, with several initiatives underway, although currently there is no centralized database to deposit raw NMR data. The Biological Magnetic Resonance Data Bank (BMRB) accepts chemical shifts, distance and orientational restraints for biological NMR data. Similar centralized resources will likely become available for small-molecule and materials NMR data. In the meantime, data can be conveniently deposited with services such as Zenodo. At present, we recommend that raw data be deposited in the JCAMP-DX version 6.0 standard, together with the original commercial format (for example, TopSpin) data and that data be made available under the CC BY 4.0 (Creative Commons Attribution-ShareAlike 4.0 International) licence.

Deposition of structural data
NMR spectroscopy-derived structures can be deposited in several databases (TABLE 2), including the Protein Data Bank (PDB) (>15,000 entries) and the BMRB for biological molecules, the Cambridge Structural Database (CSD)

(>1,000,000 entries) for organic and metal–organic solids, and the Inorganic Crystal Structure Database (ICSD) (>200,000 entries) for purely inorganic solids.

Limitations and optimizations

NMR sensitivity and resolution

The main challenge of NMR spectroscopy is its low sensitivity. Significant advances in this area include the development of DNP and ^{1}H-detected experiments under fast MAS (up to ~170 kHz)[287]. Compared with ^{13}C-detected experiments, ^{1}H detection can increase the experimental sensitivity by eightfold, which enables the measurement of high-resolution and high-sensitivity ^{1}H NMR spectra of undeuterated systems with high sensitivity[44,288]. Nevertheless, challenges remain. ^{1}H spectral resolution of solids is still a factor of 10–100 worse than solution NMR spectra. Most DNP experiments achieve their maximum sensitivity enhancements at cryogenic temperatures of 20–110 K where the electron relaxation time is sufficiently long for polarization transfer to nuclei[99]. At these cryogenic temperatures, disordered systems manifest much broader linewidths than at room temperature, thus causing spectral overlap unless the number of chemically distinct sites is low. Moreover, the efficiency of polarization in continuous-wave cross-effect DNP experiments scales unfavourably with B_0, making high-field DNP (>9.4 T) a challenge. As a result, DNP NMR spectroscopy has so far been more readily applicable to materials research[102] than to biological systems.

Spectral interpretation and refinement

For many solid-state NMR spectra, spectral resolution limits the amount of structural information obtainable. This is particularly true for disordered materials and for quadrupolar nuclei, where spectral overlap is common[140]. Spectral fitting can ameliorate this problem, but there are limitations to the accuracy of multi-parameter multi-site fits unless variable field measurements or prior information is available. In many cases, particularly for

anisotropically broadened line shapes, ideal line shapes are not relevant and simulation programs that include the exact effect of radiofrequency pulses on the density matrix (and, ultimately, on the spectrum) need to be used[142]. For quadrupolar nuclei, the complex spin dynamics means that many experiments produce qualitative rather than quantitative information, for example, giving relative proximities rather than exact distances.

Similarly, spectral overlap in protein samples complicates structural analysis. Overlap of ^{15}N chemical shifts limits the reliability of chemical shift assignment, in particular for assignment strategies that rely on NCACX and NCACX experiments. Semi-automated assignment programs have been developed to ameliorate this assignment ambiguity[289–292].

DFT calculations can greatly aid in the interpretation of the NMR spectra of materials, through the prediction of both quadrupolar and shielding parameters, but the accuracy of these calculations are limited by the methods and the functional used. Typically, generalized gradient approximation approaches are the method of choice for condensed matter simulations[149,150,293]. In principle, hybrid functionals offer improved accuracy, and some (for example, B3LYP) are widely used in molecular systems and have been shown to improve predicted ^{13}C NMR spectra of molecular crystals[294]. Although these functionals come with considerable computational costs, particularly in a periodic approach, recent developments in fragment-based techniques have demonstrated a route to exploit the benefits of hybrid functionals in solids while ensuring a reasonable computational cost[294]. More generally, the biggest limitation of using predicted NMR spectra to solve or refine structures is the time and cost of the calculation, which poses challenges to a real-time automated solution. To address this problem, machine learning approaches have been introduced to calculate chemical shifts in molecular solids that reduce computational cost by orders of magnitude while maintaining the accuracy of DFT[295].

Table 2 | **Databases for the deposition of solid-state NMR spectroscopy results**

Database	Utility	Data type	Data format	Entry requirements
Protein Data Bank (PDB)	3D structures of molecules	Macromolecular structure	PDB file format Pdb_extract can be used to extract data from your data file into the PDB format	NMR depositions require one coordinate file, one chemical shift file and at least one restraint file. Depositors are also encouraged to upload a peak list file
Biological Magnetic Resonance Data Bank (BRMB)	Data from NMR spectroscopy on biomolecules	NMR spectral parameters, relaxation data, kinetic data, thermodynamic data	NMR-STAR	When preparing a chemical shift table for NMR structure deposition, residue and atom names need to match those in the coordinates
Inorganic Crystal Structure Database (ICSD)	Atomic structure of inorganic solids	Atomic coordinates of solids	CIF	CIF containing formula, space group, size and shape of unit cell and atomic coordinates. Information usually obtained from diffraction, but often combination of diffraction and NMR
Cambridge Structural Database (CSD)	Small-molecule organic and metal–organic crystal structures	Atomic coordinates	CIF	CIF containing formula, space group, size and shape of unit cell and atomic coordinates

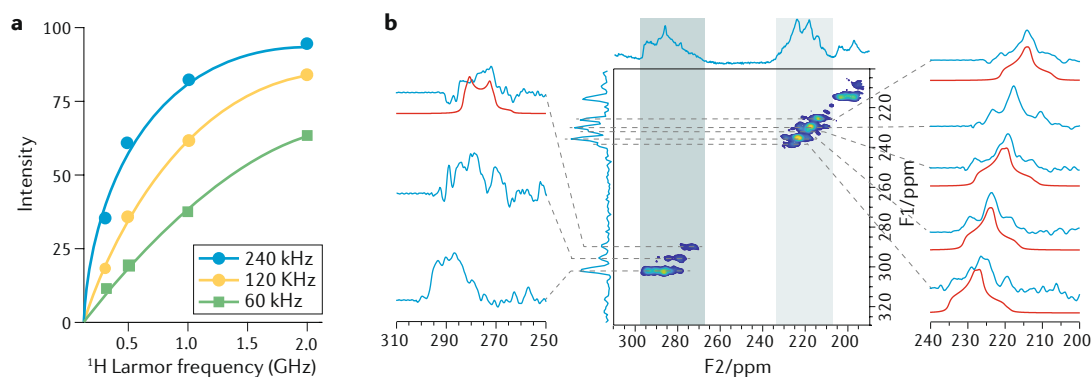CIF, crystallographic information file; NMR, nuclear magnetic resonance.

Fig. 6 | **Outlook for MAS solid-state NMR spectroscopy. a** | Sensitivities of methyl ^{1}H resonances of a typical selectively methyl protonated protein (V44γ1 from α-spectrin SH3) as a function of magnetic field strength expressed as ^{1}H Larmor frequencies[298]. These sensitivities were measured at different magic-angle spinning (MAS) rates. **b** | Quadrupolar nuclear magnetic resonance (NMR) line shapes of an ^{17}O-enriched metal–organic framework measured using a 35 T series-connected hybrid magnet illustrate the potential of high magnetic fields[323]. Blue and red solid lines indicate experimental and simulated line shapes, respectively. Areas on spectrum highlighted green and yellow correspond to different ^{17}O nuclei. ppm, parts per million. Part **a** adapted with permission from REF.[298], ACS. Part **b** reprinted with permission from REF.[323], ACS.

Outlook

Higher magnetic fields and faster MAS

Higher magnetic fields and faster MAS have consistently opened up new doors in solid-state NMR spectroscopy in the past, and we expect they will continue to do so in the future. Ultra-high magnetic fields that are equivalent to 1.2–1.5 GHz in ^{1}H Larmor frequency are becoming available through the construction of hybrid low-temperature and high-temperature superconducting magnets[296] and series-connected hybrid magnets[297]. These ultra-high magnetic fields simultaneously enhance spectral sensitivity and resolution (FIG. 6). Spectral sensitivity scales with $B_0^{3/2}$ and spectral linewidths scale with $1/B_0$ for homogeneously broadened resonances. For protons, sensitivity gains beyond the $B_0^{3/2}$ factor are expected when the isotropic chemical shift difference exceeds the ^{1}H–^{1}H dipolar coupling strength[298]. Quadrupolar nuclei further benefit from high magnetic fields as a result of the resolution enhancement due to the scaling of second-order quadrupolar interactions inversely with B_0 (REFS[33,140,263,299]). Even when the magnetic field is not high enough to reduce the quadrupolar broadening to fully resolve all sites, multi-field experiments are advantageous for extracting structurally informative NMR parameters.

Similar to higher magnetic fields, faster MAS has historically led to higher resolution and more informative solid-state NMR spectra. The maximum achievable MAS frequencies are currently limited by the speed of sound at the rotor surface[300], and thus higher rates can be achieved only for ever smaller-diameter rotors. This appears to lead to a severe reduction in sensitivity, with a 0.7 mm rotor, for example, only containing ~1 mg of sample[301]. However, as the detection efficiency, the relaxation times that are effective during the INEPT experiment and the cross-polarization experiment all increase in smaller rotors[50], experimentally, small fast-spinning samples give rise to similar sensitivities to large slower-spinning samples[44]. It has been predicted that this trend will hold up to MAS rates of ~300 kHz (REF.[302]) (FIG. 6). Faster MAS may also be achieved by

exploring rotors with non-cylindrical geometries[303]. Recently, fast MAS has been shown to enhance the sensitivity of DNP NMR experiments[288,304]: for example, results from 0.7 mm rotors spinning at 65 kHz show twofold higher DNP enhancements simply due to higher spinning rates, yielding sensitivity enhancements of 200 at high field (21.1 T). The combination of fast MAS and DNP thus opens up the possibility of ^{1}H-detected MAS DNP.

Further development in DNP NMR

Most current continuous-wave DNP experiments are conducted at cryogenic temperatures and moderate magnetic fields to obtain high-sensitivity enhancements. Key future directions include the development of pulsed DNP techniques[305] to increase the sensitivity gains at high fields, with the concomitant improvement of spectral resolution[306], and the development of new polarizing strategies suitable for ambient temperatures.

New NMR methods

Continued advances in solid-state NMR spectroscopy will benefit from the discovery of conceptually novel experimental methods. Many of these new pulse sequences are expected to capitalize on the increased resolution and coherence lifetimes enabled by faster MAS, higher magnetic fields and the increased polarization available from DNP. New methods to measure distances and large-amplitude motions under these high-field and fast-MAS conditions will be especially desirable[39,40].

For quadrupolar nuclei, future challenges lie in the measurement of high-resolution and high-sensitivity spectra and the extraction of more quantitative information[30,140]. Here, we expect to see completely new approaches to provide the step change in sensitivity. For extracting quantitative structural information from NMR experiments, we expect that the rapid advances in computational methods will enable large-scale calculations of NMR parameters and artificial intelligence-based spectral interpretation for direct output of molecular or materials properties.

Solid-state NMR spectroscopy is particularly dependent on the development of probe technology. In addition to faster MAS, multichannel NMR probes that allow simultaneous decoupling of multiple quadrupolar nuclei will be beneficial for enhancing the spectral resolution of inorganic materials. This instrumentation will also facilitate correlation experiments between different quadrupolar nuclei. Such experiments will require the development of more efficient polarization transfer pulse sequences, which can be aided by efficient simulation of larger spin systems[307].

In situ, in operando and in vivo

As chemistry, biology and materials sciences move away from studying pure systems towards complex systems on living or operational objects, in situ, in operando and in vivo NMR spectroscopy becomes more and more attractive. We expect to see rapid development of experiments and technology in this area tailored to new applications in materials research such as catalysis, electrochemistry and solar conversion, as well as in biological chemistry research. In parallel, we expect to see an increased interest in trapping methods for ex situ NMR analysis, such as pH jump, rapid mixing and freeze quenching[308]. Some of these trapping protocols will be combined with DNP NMR spectroscopy[309]. In vivo biological studies by NMR spectroscopy[310] benefit from the non-perturbing nature of NMR and its capability to detect both immobilized and dynamic molecules in cells quantitatively. Emerging topics include bacterial and mammalian extracellular matrices[219,311], protein folding and misfolding in mammalian cells[312] and membrane proteins in native membranes[313,314].

High pressure and temperature

Measurements at temperatures and pressures that are higher than currently available are imperative for many applications in catalysis and materials science. Further miniaturization will be required to enable experiments in smaller and faster-spinning rotors[94]. Performing solid-state NMR experiments at higher pressure will require significant development of new instrumentation, such as possibly integrating miniature diamond anvil cells within an MAS rotor.

Miniaturization

Another direction that could enable new applications is related to miniaturization of solid-state NMR systems. This potentially includes micrometre-sized rotors arising from new geometries for MAS[300] and the reduction in size of NMR magnets and probes from the current 1 m scale to the centimetre range[315]. Such developments could transform the ability to carry out in situ

measurements. The possibility to conduct solid-state NMR experiments in open-faced systems with spinning magnets[316,317] instead of spinning samples is also being explored to enable NMR measurements in many industrial and operando settings.

New horizons

The methodological advances discussed above will expand the applications of solid-state NMR spectroscopy to many emerging fields where atomic-level characterization is vital but where few other analytical methods are available. For example, in chemical biology, increasing interest in mapping brain functions invites the application of solid-state NMR for studying protein–RNA interactions; the structurally poorly understood yet disease-significant glycan layers of pathogens and cancer cells call for comprehensive studies of carbohydrate–protein interactions; the central role of the proteostasis network in diseases suggests that solid-state NMR studies of the time course of protein folding and misfolding will likely be of interest; and challenges in drug delivery compel solid-state NMR studies of systems such as lipid nanoparticles. In these applications, we expect solid-state NMR spectroscopy to be increasingly integrated with biochemical techniques and to complement other methods by providing atomic-scale structural, dynamical and chemical information. In materials science, we envision solid-state NMR spectroscopy to play an increasing role in discovering new materials, in addition to characterizing materials. Such discovery processes require atomic probes of complex multiscale heterogeneous architectures, which NMR is well positioned to provide. We expect conventional solid-state NMR spectroscopy to operate in parallel with new approaches for in situ and in operando online analysis, for example, combining miniaturized solid-state NMR systems with artificial intelligence-controlled discovery laboratories.

Conclusions

We have highlighted the major practices of contemporary solid-state NMR experiments and data analysis and have illustrated how these experiments are applied to biological and materials chemistry research. The exquisite control of nuclear spin coherence available to researchers, through an unlimited number of radiofrequency pulse sequences, allows scientists to extract multifaceted information from NMR data. This information spans not only static 3D structure but also dynamics, chemical composition, intermolecular interactions, structural disorder and the relation of these atomic and molecular properties to function.

Published online: 14 January 2021

1. Levitt, M. H. *Spin Dynamics Basic of Nuclear Magnetic Resonance* (Wiley, 2008).
2. Schmidt-Rohr, K. & Spiess, H. W. *Multidimensional Solid-State NMR and Polymers* Vol. 478 (Academic, 1994).
3. Facelli, J. C. Chemical shift tensors: theory and application to molecular structural problems. *Prog. Nucl. Magn. Reson. Spectrosc.* **58**, 176–201 (2011).

4. Keeler, J. *Understanding NMR Spectroscopy* (Wiley, 2011).
5. Andrew, E. R., Bradbury, A. & Eades, R. G. Nuclear magnetic resonance spectra from a crystal rotated at high speed. *Nature* **182**, 1659–1659 (1958).
6. Schaefer, J. & Stejskal, E. O. C13 nuclear magnetic resonance of polymers spinning at magic angle. *J. Am. Chem. Soc.* **98**, 1031–1032 (1976).

7. Duer, M. J. *Introduction to Solid-State NMR Spectroscopy* (Blackwell Science, 2004).
8. Hong, M. & Jakes, K. Selective and extensive ¹³C labeling of a membrane protein for solid-state NMR investigation. *J. Biomol. NMR* **14**, 71–74 (1999).
9. Tugarinov, V., Kanelis, V. & Kay, L. E. Isotope labeling strategies for the study of high-molecular-weight proteins by solution NMR spectroscopy. *Nat. Protoc.* **1**, 749–754 (2006).

10. Kainosho, M. et al. Optimal isotope labelling for NMR protein structure determinations. *Nature* **440**, 52–57 (2006).

11. Lu, J. et al. Molecular structure of β-amyloid fibrils in Alzheimer's disease brain tissue. *Cell* **154**, 1257–1268 (2013).
    This paper describes the first structural determination of brain-derived Alzheimer disease Aβ fibrils using NMR spectroscopy and brain-seeded fibrils.

12. Ashbrook, S. E. & Smith, M. E. Solid state O-17 NMR — an introduction to the background principles and applications to inorganic materials. *Chem. Soc. Rev.* **35**, 718–735 (2006).

13. Pines, A., Gibby, M. G. & Waugh, J. S. Proton-enhanced NMR of dilute spins in solids. *J. Chem. Phys.* **59**, 569–590 (1973).

14. Herzfeld, J. & Berger, A. E. Sideband intensities in NMR spectra of samples spinning at the magic angle. *J. Chem. Phys.* **73**, 6021 (1980).

15. Bielecki, A., Kolbert, A. C. & Levitt, M. H. Frequency-switched pulse sequences: homonuclear decoupling and dilute spin NMR in solids. *Chem. Phys. Lett.* **155**, 341–346 (1989).

16. Mote, K. R., Agarwal, V. & Madhu, P. K. Five decades of homonuclear dipolar decoupling in solid-state NMR: status and outlook. *Prog. Nucl. Magn. Reson. Spectrosc.* **97**, 1–39 (2016).

17. Paruzzo, F. M. & Emsley, L. High-resolution ¹H NMR of powdered solids by homonuclear dipolar decoupling. *J. Magn. Reson.* **309**, 106598 (2019).

18. Perras, F. A., Goh, T. W., Wang, L. L., Huang, W. & Pruski, M. Enhanced ¹H-X D-HMQC performance through improved ¹H homonuclear decoupling. *Solid State Nucl. Magn. Reson.* **98**, 12–18 (2019).

19. Barbet-Massin, E. et al. Rapid proton-detected NMR assignment for proteins with fast magic angle spinning. *J. Am. Chem. Soc.* **136**, 12489–12497 (2014).

20. Takegoshi, K., Nakamura, S. & Terao, T. C-13–H-1 dipolar-assisted rotational resonance in magic-angle spinning NMR. *Chem. Phys. Lett.* **344**, 631–637 (2001).

21. Bax, A., Freeman, R. & Kempsell, S. P. Natural-abundance ¹³C–¹³C coupling observed via double-quantum coherence. *J. Am. Chem. Soc.* **102**, 4849–4851 (1980).

22. Lesage, A., Bardet, M. & Emsley, L. Through-bond carbon–carbon connectivities in disordered solids by NMR. *J. Am. Chem. Soc.* **121**, 10987–10993 (1999).

23. Harris, R. K. Applications of solid-state NMR to pharmaceutical polymorphism and related matters. *J. Pharm. Pharmacol.* **59**, 225–239 (2007).

24. King, I. J., Fayon, F., Massiot, D., Harris, R. K. & Evans, J. S. O. A space group assignment of ZrP₂O₇ obtained by P-31 solid state NMR. *Chem. Commun.* **18**, 1766–1767 (2001).

25. Cadars, S., Lesage, A. & Emsley, L. Chemical shift correlations in disordered solids. *J. Am. Chem. Soc.* **127**, 4466–4476 (2005).

26. De Paëpe, G. Dipolar recoupling in magic angle spinning solid-state nuclear magnetic resonance. *Annu. Rev. Phys. Chem.* **63**, 661–684 (2012).

27. Terao, T., Miura, H. & Saika, A. I–S dipolar switching-angle spinning 2D NMR (SLF). *J. Chem. Phys.* **85**, 3816–3826 (1986).

28. Mueller, K. T. et al. Dynamic-angle spinning of quadrupolar nuclei. *J. Magn. Reson.* **86**, 470 (1990).

29. Apperley, D. C., Harris, R. K. & Hodgkinson, P. *Solid-state NMR: Basic Principles and Practice* (Momentum, 2012).

30. Ashbrook, S. E. & Sneddon, S. New methods and applications in solid-state NMR spectroscopy of quadrupolar nuclei. *J. Am. Chem. Soc.* **136**, 15440–15456 (2014).

31. Gan, Z., Gor'kov, P., Cross, T. A., Samoson, A. & Massiot, D. Seeking higher resolution and sensitivity for NMR of quadrupolar nuclei at ultrahigh magnetic fields. *J. Am. Chem. Soc.* **124**, 5634–5635 (2002).

32. Frydman, L. & Harwood, J. S. Isotropic spectra of half-integer quadrupolar spins from bidimensional magic-angle-spinning NMR. *J. Am. Chem. Soc.* **117**, 5367–5368 (1995).
    This paper revolutionizes the structural study of quadrupolar nuclei in many materials by removing the line broadening that affects the solid-state NMR spectra.

33. Schurko, R. W. Ultra-wideline solid-state NMR spectroscopy. *Acc. Chem. Res.* **46**, 1985–1995 (2013).

34. Spiess, H. W. ²H NMR for studying mobility and orientation in polymers. *Adv. Polym. Sci.* **66**, 23–56 (1985).

35. Davis, J. H. The description of membrane lipid conformation, order and dynamics by ²H-NMR. *Biochim. Biophys. Acta* **737**, 117–171 (1983).

36. Petrache, H. I., Dodd, S. W. & Brown, M. F. Area per lipid and acyl length distributions in fluid phosphatidylcholines determined by H-2 NMR spectroscopy. *Biophys. J.* **79**, 3172–3192 (2000).

37. Kamp, F. et al. Bexarotene binds to the amyloid precursor protein transmembrane domain, alters its α-helical conformation, and inhibits γ-secretase nonselectively in liposomes. *ACS Chem. Neurosci.* **9**, 1702–1713 (2018).

38. Hologne, M., Faelber, K., Diehl, A. & Reif, B. Characterization of dynamics of perdeuterated proteins by MAS solid-state NMR. *J. Am. Chem. Soc.* **127**, 11208–11209 (2005).

39. Shi, X. Y. & Rienstra, C. M. Site-specific internal motions in GB1 protein microcrystals revealed by 3D ²H–¹³C–¹³C solid-state NMR spectroscopy. *J. Am. Chem. Soc.* **138**, 4105–4119 (2016).

40. Gelenter, M. D., Wang, T., Liao, S. Y., O'Neill, H. & Hong, M. ²H–¹³C correlation solid-state NMR for investigating dynamics and water accessibilities of proteins and carbohydrates. *J. Biomol. NMR* **68**, 257–270 (2017).

41. Comellas, G. & Rienstra, C. M. Protein structure determination by magic-angle spinning solid-state NMR, and insights into the formation, structure, and stability of amyloid fibrils. *Annu. Rev. Biophys.* **42**, 515–536 (2013).

42. Chevelkov, V., Rehbein, K., Diehl, A. & Reif, B. Ultra-high resolution in proton solid-state NMR at high levels of deuteration. *Angew. Chem. Int. Ed.* **45**, 3878–3881 (2006).
    This paper reports the first demonstration of high-resolution ¹H correlation solid-state NMR spectra.

43. Penzel, S. et al. Protein resonance assignment at MAS frequencies approaching 100 kHz: a quantitative comparison of J-coupling and dipolar-coupling-based transfer methods. *J. Biomol. NMR* **63**, 165–186 (2015).

44. Andreas, L. B. et al. Structure of fully protonated proteins by proton-detected magic-angle spinning NMR. *Proc. Natl Acad. Sci. USA* **113**, 9187–9192 (2016).
    This paper describes the first de novo structure obtained from ¹H-detected solid-state NMR experiments.

45. Xiang, S. et al. Sequential backbone assignment based on dipolar amide-to-amide correlation experiments. *J. Biomol. NMR* **62**, 303–311 (2015).

46. Schanda, P., Huber, M., Verel, R., Ernst, M. & Meier, B. H. Direct detection of ³ʰJ(NC') hydrogen-bond scalar couplings in proteins by solid-state NMR spectroscopy. *Angew. Chem. Int. Ed.* **48**, 9322–9325 (2009).

47. Hiller, S., Wasmer, C., Wider, G. & Wuthrich, K. Sequence-specific resonance assignment of soluble nonglobular proteins by 7D APSY-NMR spectroscopy. *J. Am. Chem. Soc.* **129**, 10823–10828 (2007).

48. Mobli, M. & Hoch, J. C. Nonuniform sampling and non-Fourier signal processing methods in multidimensional NMR. *Prog. Nucl. Magn. Reson. Spectrosc.* **83**, 21–41 (2014).

49. Paramasivam, S. et al. Enhanced sensitivity by nonuniform sampling enables multidimensional MAS NMR spectroscopy of protein assemblies. *J. Phys. Chem. B* **116**, 7416–7427 (2012).

50. Orton, H. W. et al. Protein NMR resonance assignment without spectral analysis: 5D solid-state automated projection spectroscopY (SO-APSY). *Angew. Chem. Int. Ed.* **59**, 2380–2384 (2020).

51. Schmidt, E. & Guntert, P. A new algorithm for reliable and general NMR resonance assignment. *J. Am. Chem. Soc.* **134**, 12817–12829 (2012).

52. Tycko, R. On the problem of resonance assignments in solid state NMR of uniformly N-15, C-13-labeled proteins. *J. Magn. Reson.* **253**, 166–172 (2015).

53. Stanek, J. et al. Automated backbone NMR resonance assignment of large proteins using redundant linking from a single simultaneous acquisition. *J. Am. Chem. Soc.* **142**, 5793–5799 (2020).

54. Hong, M. & Schmidt-Rohr, K. Magic-angle-spinning NMR techniques for measuring long-range distances in biological macromolecules. *Acc. Chem. Res.* **46**, 2154–2163 (2013).

55. Castellani, F. et al. Structure of a protein determined by solid-state magic-angle spinning NMR spectroscopy. *Nature* **420**, 98–102 (2002).
    This report demonstrates the first complete protein structure determined by solid-state NMR spectroscopy.

56. Grommek, A., Meier, B. H. & Ernst, M. Distance information from proton-driven spin diffusion under MAS. *Chem. Phys. Lett.* **427**, 404–409 (2006).

57. Linser, R., Bardiaux, B., Higman, V., Fink, U. & Reif, B. Structure calculation from unambiguous long-range amide and methyl ¹H–¹H distance restraints for a microcrystalline protein with MAS solid-state NMR spectroscopy. *J. Am. Chem. Soc.* **133**, 5905–5912 (2011).

58. Roos, M., Wang, T., Shcherbakov, A. A. & Hong, M. Fast magic-angle-spinning ¹⁹F spin exchange NMR for determining nanometer ¹⁹F–¹⁹F distances in proteins and phamaceutical compounds. *J. Phys. Chem. B* **122**, 2900–2911 (2018).

59. Gullion, T. & Schaefer, J. Rotational echo double resonance NMR. *J. Magn. Reson.* **81**, 196–200 (1989).

60. Cegelski, L. REDOR NMR for drug discovery. *Bioorg. Med. Chem. Lett.* **23**, 5767–5775 (2013).

61. Jaroniec, C. P., Filip, C. & Griffin, R. G. 3D TEDOR NMR experiments for the simultaneous measurement of multiple carbon–nitrogen distances in uniformly ¹³C, ¹⁵N-labeled solids. *J. Am. Chem. Soc.* **124**, 10728–10742 (2002).

62. Tang, M., Waring, A. J. & Hong, M. Phosphate-mediated arginine insertion into lipid membranes and pore formation by a cationic membrane peptide from solid-state NMR. *J. Am. Chem. Soc.* **129**, 11438–11446 (2007).

63. Yang, H. et al. REDOR NMR reveals multiple conformers for a protein kinase C ligand in a membrane environment. *ACS Cent. Sci.* **4**, 89–96 (2018).

64. Elkins, M. R. et al. Cholesterol-binding site of the influenza M2 protein in lipid bilayers from solid-state NMR. *Proc. Natl Acad. Sci. USA* **114**, 12946–12951 (2017).

65. Brus, J. et al. Structure of framework aluminum Lewis sites and perturbed aluminum atoms in zeolites as determined by ²⁷Al{¹H} REDOR (3Q) MAS NMR spectroscopy and DFT/molecular mechanics. *Angew. Chem. Int. Ed. Engl.* **54**, 541–545 (2015).

66. Peng, L., Liu, Y., Kim, N., Readman, J. E. & Grey, C. P. Detection of Brønsted acid sites in zeolite HY with high-field ¹⁷O-MAS-NMR techniques. *Nat. Mater.* **4**, 216–219 (2005).

67. Shcherbakov, A. A. & Hong, M. Rapid measurement of long-range distances in proteins by multidimensional ¹³C–¹⁹F REDOR NMR under fast magic-angle spinning. *J. Biomol. NMR* **71**, 31–43 (2018).

68. Shcherbakov, A. A., Mandala, V. S. & Hong, M. High-sensitivity detection of nanometer ¹H–¹⁹F distances for protein structure determination by ¹H-detected fast MAS NMR. *J. Phys. Chem. B* **123**, 4387–4391 (2019).

69. Wang, M. et al. Fast magic angle spinning ¹⁹F NMR of HIV-1 capsid protein assemblies. *Angew. Chem. Int. Ed.* **57**, 16375–16379 (2018).

70. Ruiz-Preciado, M. A. et al. Supramolecular modulation of hybrid perovskite solar cells via bifunctional halogen bonding revealed by two-dimensional ¹⁹F solid-state NMR spectroscopy. *J. Am. Chem. Soc.* **142**, 1645–1654 (2020).

71. Gilchrist, M. L. Jr et al. Measurement of interfluorine distances in solids. *J. Magn. Reson.* **152**, 1–6 (2001).

72. Steigel, A. & Spiess, H. W. *Dynamic NMR Spectroscopy* (Springer Verlag, 1978).

73. Geahigan, K. B., Meints, G. A., Hatcher, M. E., Orban, J. & Drobny, G. P. The dynamic impact of CpG methylation in DNA. *Biochemistry* **39**, 4939–4946 (2000).

74. Copié, V. et al. Deuterium solid-state nuclear magnetic resonance studies of methyl group dynamics in bacteriorhodopsin and retinal model compounds: evidence for a 6-s-*trans* chromophore in the protein. *Biochemistry* **33**, 3280–3286 (1994).

75. Munowitz, M. G., Griffin, R. G., Bodenhausen, G. & Huang, T. H. Two-dimensional rotational spin-echo NMR in solids: correlation of chemical shift and dipolar interactions. *J. Am. Chem. Soc.* **103**, 2529–2533 (1981).

76. Hong, M. et al. Coupling amplification in 2D MAS NMR and its application to torsion angle determination in peptides. *J. Magn. Reson.* **129**, 85–92 (1997).

77. deAzevedo, E. R. et al. Intermediate motions as studied by solid-state separated local field NMR experiments. *J. Chem. Phys.* **128**, 104505 (2008).

78. Hohwy, M., Jaroniec, C. P., Reif, B., Rienstra, C. M. & Griffin, R. G. Determination of local structure and relaxation properties in solid-state NMR: accurate measurement of amide N–H bond lengths and

H–N–H bond angles. *J. Am. Chem. Soc.* **122**, 3218–3219 (2000).

79. Hou, G. J., Lu, X. Y., Vega, A. J. & Polenova, T. Accurate measurement of heteronuclear dipolar couplings by phase-alternating R-symmetry (PARS) sequences in magic angle spinning NMR spectroscopy. *J. Chem. Phys.* **141**, e104202 (2014).

80. van Rossum, B.-J., de Groot, C. P., Ladizhansky, V., Vega, S. & de Groot, H. J. M. A method for measuring heteronuclear (^{1}H–^{13}C) distances in high speed MAS NMR. *J. Am. Chem. Soc.* **122**, 3465–3472 (2000).

81. Schanda, P., Huber, M., Boisbouvier, J., Meier, B. H. & Ernst, M. Solid-state NMR measurements of asymmetric dipolar couplings provide insight into protein side-chain motion. *Angew. Chem. Int. Ed.* **50**, 11005–11009 (2011).

82. Asami, S. & Reif, B. Comparative study of REDOR and CPPI derived order parameters by ^{1}H-detected MAS NMR and MD simulations. *J. Phys. Chem. B* **121**, 8719–8730 (2017).

83. Xue, K., Mühlbauer, M., Mamone, S., Sarkar, R. & Reif, B. Accurate determination of ^{1}H–^{15}N dipolar couplings using inaccurate settings of the magic angle in solid-state NMR spectroscopy. *Angew. Chem. Int. Ed.* **58**, 4286–4290 (2019).

84. Paluch, P. et al. Theoretical study of CP-VC: a simple, robust and accurate MAS NMR method for analysis of dipolar C–H interactions under rotation speeds faster than ca. 60 kHz. *J. Magn. Res.* **252**, 67–77 (2015).

85. deAzevedo, E. R., Bonagamba, T. J., Hu, W. & Schmidt-Rohr, K. Centerband-only detection of exchange: efficient analysis of dynamics in solids by NMR. *J. Am. Chem. Soc.* **121**, 8411–8412 (1999).

86. Krushelnitsky, A. et al. Direct observation of milliseconds to second motions in proteins by dipolar CODEX NMR spectroscopy. *J. Am. Chem. Soc.* **131**, 12097–12099 (2009).

87. Giraud, N. et al. Quantitative analysis of backbone dynamics in a crystalline protein from nitrogen-15 spin-lattice relaxation. *J. Am. Chem. Soc.* **127**, 18190–18201 (2005).

88. Chevelkov, V., Diehl, A. & Reif, B. Measurement of ^{15}N-T$_1$ relaxation rates in a perdeuterated protein by MAS solid-state NMR spectroscopy. *J. Chem. Phys.* **128**, 052316 (2008).

89. Lewandowski, J. R., Sass, H. J., Grzesiek, S., Blackledge, M. & Emsley, L. Site-specific measurement of slow motions in proteins. *J. Am. Chem. Soc.* **133**, 16762–16765 (2011).

90. Rovo, P. & Linser, R. Microsecond timescale protein dynamics: a combined solid-state NMR approach. *ChemPhysChem* **19**, 34–39 (2018).

91. Marion, D., Gauto, D. F., Ayala, I., Giandoreggio-Barranco, K. & Schanda, P. Microsecond protein dynamics from combined Bloch–McConnell and near-rotary-resonance R$_{1\rho}$ relaxation-dispersion MAS NMR. *ChemPhysChem* **20**, 276–284 (2019).

92. Giraud, N., Blackledge, M., Böckmann, A. & Emsley, L. The influence of nitrogen-15 proton-driven spin diffusion on the measurement of nitrogen-15 longitudinal relaxation times. *J. Magn. Reson.* **184**, 51–61 (2007).

93. Phan, V., Fry, E. A. & Zilm, K. W. Accounting for the temperature dependence of C-13 spin-lattice relaxation of methyl groups in the glycyl-alanyl-leucine model system under MAS with spin diffusion. *J. Biomol. NMR* **73**, 411–421 (2019).

94. Kirchhain, H. & van Wullen, L. Solid state NMR at very high temperatures. *Prog. Nucl. Magn. Reson. Spectrosc.* **114**, 71–85 (2019).

95. Meier, T. et al. NMR at pressures up to 90 GPa. *J. Magn. Res.* **292**, 44–47 (2018).

96. Chamas, A. et al. High temperature/pressure MAS-NMR for the study of dynamic processes in mixed phase systems. *Magn. Reson. Imaging* **56**, 37–44 (2019).

97. Overhauser, A. W. Polarization of nuclei in metals. *Phys. Rev.* **92**, 411–415 (1953).

98. Carver, T. R. & Slichter, C. P. Polarization of nuclear spins in metals. *Phys. Rev.* **92**, 212–213 (1953).

99. Ni, Q. Z. et al. High frequency dynamic nuclear polarization. *Acc. Chem. Res.* **46**, 1933–1941 (2013).

100. Lilly Thankamony, A. S., Wittmann, J. J., Kaushik, M. & Corzilius, B. Dynamic nuclear polarization for sensitivity enhancement in modern solid-state NMR. *Prog. Nucl. Magn. Reson. Spectrosc.* **102–103**, 120–195 (2017).

101. Bajaj, V. S. et al. Dynamic nuclear polarization at 9 T using a novel 250 GHz gyrotron microwave source. *J. Magn. Reson.* **160**, 85–90 (2003).

102. Rossini, A. J. et al. Dynamic nuclear polarization surface enhanced NMR spectroscopy. *Acc. Chem. Res.* **46**, 1942–1951 (2013).

103. Lesage, A. et al. Surface enhanced NMR spectroscopy by dynamic nuclear polarization. *J. Am. Chem. Soc.* **132**, 15459–15461 (2010).
This is the first paper introducing impregnation DNP and showing how it can enable the study of surface structures of materials, using nanoporous silica material as an example.

104. Sauvée, C. et al. Highly efficient, water-soluble polarizing agents for dynamic nuclear polarization at high frequency. *Angew. Chem. Int. Ed. Engl.* **52**, 10858–10861 (2013).

105. Zagdoun, A. et al. Large molecular weight nitroxide biradicals providing efficient dynamic nuclear polarization at temperatures up to 200 K. *J. Am. Chem. Soc.* **135**, 12790–12797 (2013).

106. Bertini, I., Luchinat, C., Parigi, G. & Ravera, E. *NMR of Paramagnetic Molecules: Applications to Metallobiomolecules and Models* 2nd edn (Elsevier Science BV, 2017).

107. Pell, A. J., Pintacuda, G. & Grey, C. P. Paramagnetic NMR in solution and the solid state. *Prog. Nucl. Magn. Reson. Spectrosc.* **111**, 1–271 (2019).

108. Solomon, I. Relaxation processes in a system of two spins. *Phys. Rev.* **99**, 559–565 (1955).

109. Buffy, J. J. et al. Solid-state NMR investigation of the depth of insertion of protegin-1 in lipid bilayers using paramagnetic Mn^{2+}. *Biophys. J.* **85**, 2363–2373 (2003).

110. Parthasarathy, S. et al. Molecular-level examination of Cu^{2+} binding structure for amyloid fibrils of 40-residue Alzheimer's β by solid-state NMR spectroscopy. *J. Am. Chem. Soc.* **133**, 3390–3400 (2011).

111. Nadaud, P. S., Helmus, J. J., Sengupta, I. & Jaroniec, C. P. Rapid acquisition of multidimensional solid-state NMR spectra of proteins facilitated by covalently bound paramagnetic tags. *J. Am. Chem. Soc.* **132**, 9561–9563 (2010).

112. Öster, C. et al. Characterization of protein–protein interfaces in large complexes by solid-state NMR solvent paramagnetic relaxation enhancements. *J. Am. Chem. Soc.* **139**, 12165–12174 (2017).

113. Knight, M. J. et al. Structure and backbone dynamics of a microcrystalline metalloprotein by solid-state NMR. *Proc. Natl Acad. Sci. USA* **109**, 11095–11100 (2012).

114. Wickramasinghe, N. P. et al. Nanomole-scale protein solid-state NMR by breaking intrinsic ^{1}HT$_1$ boundaries. *Nat. Methods* **6**, 215–218 (2009).

115. Wu, X. L. & Zilm, K. W. Complete spectral editing in CPMAS NMR. *J. Magn. Reson. A* **102**, 205–213 (1993).

116. Schmidt-Rohr, K. & Mao, J. D. Efficient CH-group selection and identification in C-13 solid-state NMR by dipolar DEPT and H-1 chemical-shift filtering. *J. Am. Chem. Soc.* **124**, 13938–13948 (2002).

117. Mao, J. D. & Schmidt-Rohr, K. Methylene spectral editing in solid-state C-13 NMR by three-spin coherence selection. *J. Magn. Reson.* **176**, 1–6 (2005).

118. Rienstra, C. M., Hohwy, M., Hong, M. & Griffin, R. G. 2D and 3D ^{15}N–^{13}C–^{13}C NMR chemical shift correlation spectroscopy of solids: assignment of MAS spectra of peptides. *J. Am. Chem. Soc.* **122**, 10979–10990 (2000).

119. Baldus, M., Petkova, A. T., Herzfeld, J. & Griffin, R. G. Cross polarization in the tilted frame: assignment and spectral simplification in heteronuclear spin systems. *Mol. Phys.* **95**, 1197–1207 (1998).

120. Pauli, J., Baldus, M., Van Rossum, B.-J., De Groot, H. & Oschkinat, H. Backbone and side-chain ^{13}C and ^{15}N signal assignments of the α-spectrin SH3 domain by magic-angle spinning solid-state NMR at 17.6 Tesla. *ChemBioChem* **2**, 272–281 (2001).

121. De Paëpe, G., Lewandowski, J. R., Loquet, A., Böckmann, A. & Griffin, R. G. Proton assisted recoupling and protein structure determination. *J. Chem. Phys.* **129**, 245101 (2008).

122. Gelenter, M. D. & Hong, M. Efficient ^{15}N–^{13}C polarization transfer by third-spin-assisted pulsed cross-polarization magic-angle-spinning NMR for protein structure determination. *J. Phys. Chem. B* **122**, 8367–8379 (2018).

123. Ishii, Y. C-13–C-13 dipolar recoupling under very fast magic angle spinning in solid-state nuclear magnetic resonance: applications to distance measurements, spectral assignments, and high-throughput secondary-structure determination. *J. Chem. Phys.* **114**, 8473–8483 (2001).

124. Jaroniec, C. P., Tounge, B. A., Rienstra, C. M., Herzfeld, J. & Griffin, R. G. Recoupling of heteronuclear dipolar interactions with rotational-echo double-resonance at high magic-angle spinning frequencies. *J. Magn. Reson.* **146**, 132–139 (2000).

125. Su, Y., Hu, F. & Hong, M. Paramagnetic Cu(II) for probing membrane protein structure and function: inhibition mechanism of the influenza M2 proton channel. *J. Am. Chem. Soc.* **134**, 8693–8702 (2012).

126. Theint, T. et al. Structural studies of amyloid fibrils by paramagnetic solid-state nuclear magnetic resonance spectroscopy. *J. Am. Chem. Soc.* **140**, 13161–13166 (2018).

127. Su, Y., Mani, R. & Hong, M. Asymmetric insertion of membrane proteins in lipid bilayers by solid-state NMR paramagnetic relaxation enhancement: a cell-penetrating peptide example. *J. Am. Chem. Soc.* **130**, 8856–8864 (2008).

128. Mandala, V. S., Loftis, A. R., Shcherbakov, A. A., Pentelute, B. L. & Hong, M. Atomic structures of closed and open influenza B M2 proton channel reveal the conduction mechanism. *Nat. Struc. Mol. Biol.* **27**, 160–167 (2020).

129. Das, B. B. et al. Structure determination of a membrane protein in proteoliposomes. *J. Am. Chem. Soc.* **134**, 2047–2056 (2012).

130. Phyo, P. et al. Gradients in wall mechanics and polysaccharides along growing inflorescence stems. *Plant Physiol.* **175**, 1593–1607 (2017).

131. Williams, J. K., Zhang, Y., Schmidt-Rohr, K. & Hong, M. pH-dependent conformation, dynamics, and aromatic interaction of the gating tryptophan residue of the influenza M2 proton channel from solid-state NMR. *Biophys. J.* **104**, 1698–1708 (2013).

132. Chevelkov, V., Fink, U. & Reif, B. Accurate determination of order parameters from ^{1}H,^{15}N dipolar couplings in MAS solid-state NMR experiments. *J. Am. Chem. Soc.* **131**, 14018–14022 (2009).

133. Schanda, P., Meier, B. H. & Ernst, M. Quantitative analysis of protein backbone dynamics in microcrystalline ubiquitin by solid-state NMR spectroscopy. *J. Am. Chem. Soc.* **132**, 15957–15967 (2010).

134. Ma, P. X. et al. Observing the overall rocking motion of a protein in a crystal. *Nat. Commun.* **6**, e8361 (2015).

135. Lewandowski, J. R., Sein, J., Blackledge, M. & Emsley, L. Anisotropic collective motion contributes to nuclear spin relaxation in crystalline proteins. *J. Am. Chem. Soc.* **132**, 1246–+ (2010).

136. Lewandowski, J. R., Halse, M. E., Blackledge, M. & Emsley, L. Protein dynamics. Direct observation of hierarchical protein dynamics. *Science* **348**, 578–581 (2015).
This study provides a quantitative analysis of the coupling of protein and solvent dynamics using relaxation NMR spectroscopy.

137. Smith, A. A., Ernst, M., Riniker, S. & Meier, B. H. Localized and collective motions in HET-s(218–289) fibrils from combined NMR relaxation and MD simulation. *Angew. Chem. Int. Ed.* **58**, 9383–9388 (2019).

138. Shannon, M. D. et al. Conformational dynamics in the core of human Y145Stop prion protein amyloid probed by relaxation dispersion NMR. *ChemPhysChem* **20**, 311–317 (2019).

139. Gauto, D. F. et al. Aromatic ring dynamics, thermal activation, and transient conformations of a 468 kDa enzyme by specific H-1–C-13 labeling and fast magic-angle spinning NMR. *J. Am. Chem. Soc.* **141**, 11183–11195 (2019).

140. Wasylishen, R. E., Ashbrook, S. E. & Wimperis, S. *NMR of Quadrupolar Nuclei in Solid Materials* (Wiley, 2012).

141. Massiot, D. et al. Modelling one- and two-dimensional solid-state NMR spectra. *Magn. Reson. Chem.* **40**, 70–76 (2002).

142. Bak, M., Rasmussen, J. T. & Nielsen, N. C. SIMPSON: a general simulation program for solid-state NMR spectroscopy. *J. Magn. Res.* **147**, 296–330 (2000).

143. Ashbrook, S. E., Berry, A. J. & Wimperis, S. O-17 multiple-quantum MAS NMR study of pyroxenes. *J. Phys. Chem. B* **106**, 773–778 (2002).

144. Frydman, L. & Harwood, J. S. Isotropic spectra of half-integer quadrupolar spins from bidimensional magic-angle-spinning NMR. *J. Am. Chem. Soc.* **117**, 5367–5368 (1995).

145. Goldbourt, A. & Madhu, P. K. Multiple-quantum magic-angle spinning: high-resolution solid-state NMR of half-integer spin quadrupolar nuclei. *Annu. Rep. NMR Spec.* **54**, 81–153 (2005).

146. Moran, R. F., Dawson, D. M. & Ashbrook, S. E. Exploiting NMR spectroscopy for the study of disorder in solids. *Int. Rev. Phys. Chem.* **36**, 39–115 (2017).

147. Le Caer, G., Bureau, B. & Massiot, D. An extension of the Czjzek model for the distributions of electric field gradients in disordered solids and an application to NMR spectra of Ga-71 in chalcogenide glasses. *J. Phys. Condens. Matter* **22**, 065402 (2010).

148. Trease, N. M., Clark, T. M., Grandinetti, P. J., Stebbins, J. F. & Sen, S. Bond length–bond angle correlation in densified silica-results from O-17 NMR spectroscopy. *J. Chem. Phys.* **146**, 184505 (2017).

149. Ashbrook, S. E. & McKay, D. Combining solid-state NMR spectroscopy with first-principles calculations — a guide to NMR crystallography. *Chem. Commun.* **52**, 7186–7204 (2016).
 This review describes how to use computational prediction of NMR interactions and NMR parameters alongside experiments to help interpret and assign more complex spectral signals, thereby gaining more detailed structural insight.

150. Bonhomme, C. et al. First-principles calculation of NMR parameters using the gauge including projector augmented wave method: a chemist's point of view. *Chem. Rev.* **112**, 5733–5779 (2012).

151. Pickard, C. J. & Mauri, F. All-electron magnetic response with pseudopotentials: NMR chemical shifts. *Phys. Rev. B* **63**, 245101 (2001).
 This paper establishes the framework for accurate calculation of chemical shifts in periodic solids.

152. Caulkins, B. G. et al. NMR crystallography of a carbanionic intermediate in tryptophan synthase: chemical structure, tautomerization, and reaction specificity. *J. Am. Chem. Soc.* **138**, 15214–15226 (2016).

153. Baias, M. et al. De novo determination of the crystal structure of a large drug molecule by crystal structure prediction-based powder NMR crystallography. *J. Am. Chem. Soc.* **135**, 17501–17507 (2013).

154. Cadars, S. et al. Long- and short-range constraints for the structure determination of layered silicates with stacking disorder. *Chem. Mater.* **26**, 6994–7008 (2014).

155. Charpentier, T., Menziani, M. C. & Pedone, A. Computational simulations of solid state NMR spectra: a new era in structure determination of oxide glasses. *RSC Adv.* **3**, 10550–10578 (2013).

156. Cady, S. D. et al. Structure of the amantadine binding site of influenza M2 proton channels in lipid bilayers. *Nature* **463**, 689–692 (2010).
 This study demonstrates the first determination of the structure and dynamics of a pharmaceutical drug bound to a membrane protein.

157. Sharma, M. et al. Insight into the mechanism of the influenza A proton channel from a structure in a lipid bilayer. *Science* **330**, 509–512 (2010).

158. Lange, A. et al. Toxin-induced conformational changes in a potassium channel revealed by solid-state NMR. *Nature* **440**, 959–962 (2006).
 This study shows how high-affinity binding of the scorpion toxin to a chimeric K+ channel is associated with significant structural rearrangements in both molecules, which explains the high specificity of toxin–K+ channel interactions.

159. Wylie, B. J., Bhate, M. P. & McDermott, A. E. Transmembrane allosteric coupling of the gates in a potassium channel. *Proc. Natl Acad. Sci. USA* **111**, 185–190 (2014).

160. Öster, C. et al. The conduction pathway of potassium channels is water free under physiological conditions. *Sci. Adv.* **5**, eaaw6756 (2019).

161. Gayen, A., Leninger, M. & Traaseth, N. J. Protonation of a glutamate residue modulates the dynamics of the drug transporter EmrE. *Nat. Chem. Biol.* **12**, 141–145 (2016).

162. Lehnert, E. et al. Antigenic peptide recognition on the human ABC transporter TAP resolved by DNP-enhanced solid-state NMR spectroscopy. *J. Am. Chem. Soc.* **138**, 13967–13974 (2016).

163. Lalli, D. et al. Proton-based structural analysis of a heptahelical transmembrane protein in lipid bilayers. *J. Am. Chem. Soc.* **139**, 13006–13012 (2017).

164. Wang, S. L. et al. Solid-state NMR spectroscopy structure determination of a lipid-embedded heptahelical membrane protein. *Nat. Methods* **10**, 1007-–1012 (2013).

165. Retel, J. S. et al. Structure of outer membrane protein G in lipid bilayers. *Nat. Commun.* **8**, 2073 (2017).

166. Medeiros-Silva, J. et al. High-resolution NMR studies of antibiotics in cellular membranes. *Nat. Commun.* **9**, 3963 (2018).

167. Amani, R. et al. Conformational changes upon gating of KirBac1.1 into an open-activated state revealed by solid-state NMR and functional assays. *Proc. Natl Acad. Sci. USA* **117**, 2938–2947 (2020).

168. Mandala, V. S., Gelenter, M. D. & Hong, M. Transport-relevant protein conformational dynamics and water dynamics on multiple time scales in an Archetypal proton channel: insights from solid-state NMR. *J. Am. Chem. Soc.* **140**, 1514–1524 (2018).

169. Spadaccini, R., Kaur, H., Becker-Baldus, J. & Glaubitz, C. The effect of drug binding on specific sites in transmembrane helices 4 and 6 of the ABC exporter MsbA studied by DNP-enhanced solid-state NMR. *Biochim. Biophys. Acta* **1860**, 833–840 (2018).

170. Maciejko, J., Kaur, J., Becker-Baldus, J. & Glaubitz, C. Photocycle-dependent conformational changes in the proteorhodopsin cross-protomer Asp-His-Trp triad revealed by DNP-enhanced MAS-NMR. *Proc. Natl Acad. Sci. USA* **116**, 8342–8349 (2019).

171. Becker-Baldus, J. et al. Enlightening the photoactive site of channelrhodopsin-2 by DNP-enhanced solid-state NMR spectroscopy. *Proc. Natl Acad. Sci. USA* **112**, 9896–9901 (2015).

172. Ni, Q. Z. et al. Primary transfer step in the light-driven ion pump bacteriorhodopsin: an irreversible U-turn revealed by dynamic nuclear polarization-enhanced magic angle spinning NMR. *J. Am. Chem. Soc.* **140**, 4085–4091 (2018).

173. Good, D., Pham, C., Jagas, J., Lewandowski, J. R. & Ladizhansky, V. Solid-state NMR provides evidence for small-amplitude slow domain motions in a multispanning transmembrane α-helical protein. *J. Am. Chem. Soc.* **139**, 9246–9258 (2017).

174. Tycko, R. Amyloid polymorphism: structural basis and neurobiological relevance. *Neuron* **86**, 632–645 (2015).

175. Xiao, Y. L. et al. A β$_{1-42}$ fibril structure illuminates self-recognition and replication of amyloid in Alzheimer's disease. *Nat. Struct. Mol. Biol.* **22**, 499–505 (2015).

176. Colvin, M. T. et al. Atomic resolution structure of monomorphic Aβ$_{42}$ amyloid fibrils. *J. Am. Chem. Soc.* **138**, 9663–9674 (2016).
 This paper determines an atomic resolution structure of a monomorphic form of Aβ$_{42}$ amyloid fibrils, which is essential to the aetiology of Alzheimer disease.

177. Wälti, M. A. et al. Atomic-resolution structure of a disease-relevant Aβ$_{1-42}$ amyloid fibril. *Proc. Natl Acad. Sci. USA* **113**, E4976–E4984 (2016).

178. Bousset, L. et al. Structural and functional characterization of two α-synuclein strains. *Nat. Commun.* **4**, 2575 (2013).

179. Tuttle, M. D. et al. Solid-state NMR structure of a pathogenic fibril of full-length human α-synuclein. *Nat. Struct. Mol. Biol.* **23**, 409–415 (2016).

180. Fitzpatrick, A. W. et al. Atomic structure and hierarchical assembly of a cross-β amyloid fibril. *Proc. Natl Acad. Sci. USA* **110**, 5468–5473 (2013).

181. Iadanza, M. G. et al. The structure of a β$_2$-microglobulin fibril suggests a molecular basis for its amyloid polymorphism. *Nat. Commun.* **9**, 1–10 (2018).

182. Murray, D. T. et al. Structure of FUS protein fibrils and its relevance to self-assembly and phase separation of low-complexity domains. *Cell* **171**, 615–627 (2017).

183. Dregni, A. J. et al. In vitro 0N4R tau fibrils contain a monomorphic b-sheet core enclosed by dynamically heterogeneous fuzzy coat segments. *Proc. Natl Acad. Sci. USA* **116**, 16357–16366 (2019).

184. Piehl, D. W. et al. Immunoglobulin light chains form an extensive and highly ordered fibril involving the N- and C-termini. *ACS Omega* **2**, 712–720 (2017).

185. Hora, M. et al. Antibody light chain fibrils are similar to oligomeric precursors. *PLoS ONE* **12**, e0181799 (2017).

186. Prade, E. et al. Structural mechanism of the interaction of Alzheimer's disease Aβ fibrils with the non-steroidal anti-inflammatory drug (NSAID) sulindac sulfide. *J. Biol. Chem.* **290**, 28737–28745 (2015).

187. Lopez del Amo, J.-M. et al. Structural properties of EGCG induced, non-toxic Alzheimer's disease Aβ oligomers. *J. Mol. Biol.* **421**, 517–524 (2012).

188. Chimon, S. et al. Evidence of fibril-like β-sheet structures in a neurotoxic amyloid intermediate of Alzheimer's β-amyloid. *Nat. Struct. Mol. Biol.* **14**, 1157–1164 (2007).

189. Qiang, W., Yau, W. M. & Schulte, J. Fibrillation of β amyloid peptides in the presence of phospholipid bilayers and the consequent membrane disruption. *Biochim. Biophys. Acta* **1848**, 266–276 (2015).

190. Fusco, G. et al. Direct observation of the three regions in α-synuclein that determine its membrane-bound behaviour. *Nat. Commun.* **5**, 3827 (2014).

191. Wang, T., Jo, H., DeGrado, W. F. & Hong, M. Water distribution, dynamics, and interactions with Alzheimer's β-amyloid fibrils investigated by solid-state NMR. *J. Am. Chem. Soc.* **139**, 6242–6252 (2017).

192. Murray, D. T. & Tycko, R. Side chain hydrogen-bonding interactions within amyloid-like fibrils formed by the low-complexity domain of FUS: evidence from solid state nuclear magnetic resonance spectroscopy. *Biochemistry* **59**, 364–378 (2020).

193. Dregni, A. J., Duan, P. & Hong, M. Hydration and dynamics of full-length tau amyloid fibrils investigated by solid-state nuclear magnetic resonance. *Biochemistry* **59**, 2237–2248 (2020).

194. Wasmer, C. et al. Amyloid fibrils of the HET-s(218–289) prion form a β solenoid with a triangular hydrophobic core. *Science* **319**, 1523–1526 (2008).

195. Gelenter, M. D. et al. The peptide hormone glucagon forms amyloid fibrils with two coexisting β-strand conformations. *Nat. Struct. Mol. Biol.* **26**, 592–598 (2019).

196. Nespovitaya, N. et al. Dynamic assembly and disassembly of functional β-endorphin amyloid fibrils. *J. Am. Chem. Soc.* **138**, 846–856 (2016).

197. Bertini, I. et al. Solid-state NMR of proteins sedimented by ultracentrifugation. *Proc. Natl Acad. Sci. USA* **108**, 10396–10399 (2011).

198. Yan, S. et al. Atomic-resolution structure of the CAP-Gly domain of dynactin on polymeric microtubules determined by magic angle spinning NMR spectroscopy. *Proc. Natl Acad. Sci. USA* **112**, 14611–14616 (2015).

199. Lu, M. et al. Dynamic allostery governs cyclophilin A-HIV capsid interplay. *Proc. Natl Acad. Sci. USA* **112**, 14617–14622 (2015).

200. Mainz, A. et al. NMR spectroscopy of soluble protein complexes at one mega-dalton and beyond. *Angew. Chem. Int. Ed.* **52**, 8746–8751 (2013).

201. Kurauskas, V. et al. Sensitive proton-detected solid-state NMR spectroscopy of large proteins with selective CH3 labelling: application to the 50S ribosome subunit. *Chem. Commun.* **52**, 9558–9561 (2016).

202. Mainz, A. et al. The chaperone αB-crystallin uses different interfaces to capture an amorphous and an amyloid client. *Nat. Struct. Mol. Biol.* **22**, 898–905 (2015).

203. Felix, J. et al. Mechanism of the allosteric activation of the ClpP protease machinery by substrates and active-site inhibitors. *Sci. Adv.* **5**, eaaw3818 (2019).

204. Knight, M. J. et al. Rapid measurement of pseudocontact shifts in metalloproteins by proton-detected solid-state NMR spectroscopy. *J. Am. Chem. Soc.* **134**, 14730–14733 (2012).

205. Bertini, I. et al. High-resolution solid-state NMR structure of a 17.6 kDa protein. *J. Am. Chem. Soc.* **132**, 1032–1040 (2010).

206. Damman, R. et al. Atomic-level insight into mRNA processing bodies by combining solid and solution-state NMR spectroscopy. *Nat. Commun.* **10**, 4536 (2019).

207. Bertarello, A. et al. Picometer resolution structure of the coordination sphere in the metal-binding site in a metalloprotein by NMR. *J. Am. Chem. Soc.* **142**, 16757–16765 (2020).

208. Wang, T., Phyo, P. & Hong, M. Multidimensional solid-state NMR spectroscopy of plant cell walls. *Solid State Nucl. Magn. Reson.* **78**, 56–63 (2016).

209. Takahashi, H. et al. Solid-state NMR on bacterial cells: selective cell wall signal enhancement and resolution improvement using dynamic nuclear polarization. *J. Am. Chem. Soc.* **135**, 5105–5110 (2013).

210. Wang, T. & Hong, M. Solid-state NMR investigations of cellulose structure and interactions with matrix polysaccharides in plant primary cell walls. *J. Exp. Botany* **67**, 503–514 (2016).

211. Dick-Pérez, M. et al. Structure and interactions of plant cell-wall polysaccharides by two- and three-dimensional magic-angle-spinning solid-state NMR. *Biochemistry* **50**, 989–1000 (2011).

212. Wang, T., Yang, H., Kubicki, J. D. & Hong, M. Cellulose structural polymorphism in plant primary cell walls investigated by high-field 2D solid-state NMR spectroscopy and density functional theory calculations. *Biomacromolecules* **17**, 2210–2222 (2016).

213. Simmons, T. J. et al. Folding of xylan onto cellulose fibrils in plant cell walls revealed by solid-state NMR. *Nat. Commun.* **7**, 13902 (2016).

214. Phyo, P., Wang, T., Yang, Y., O'Neill, H. & Hong, M. Direct determination of hydroxymethyl conformations of plant cell wall cellulose using ¹H polarization transfer solid-state NMR. *Biomacromolecules* **19**, 1485–1497 (2018).

215. Wang, T. et al. Sensitivity-enhanced solid-state NMR detection of expansin's target in plant cell walls. *Proc. Natl Acad. Sci. USA* **110**, 16444–16449 (2013).

216. Kang, X. et al. Lignin–polysaccharide interactions in plant secondary cell walls revealed by solid-state NMR. *Nat. Commun.* **10**, 347 (2019).
This solid-state NMR study provides the first comprehensive molecular-level structural insights into lignin–polysaccharide interactions in plant secondary cell walls.

217. Kang, X. et al. Molecular architecture of fungal cell walls revealed by solid-state NMR. *Nat. Commun.* **9**, 2747 (2018).

218. Bougault, C., Ayala, I., Vollmer, W., Simorre, J. P. & Schanda, P. Studying intact bacterial peptidoglycan by proton-detected NMR spectroscopy at 100 kHz MAS frequency. *J. Struct. Biol.* **206**, 66–72 (2019).

219. McCrate, O. A., Zhou, X., Reichhardt, C. & Cegelski, L. Sum of the parts: composition and architecture of the bacterial extracellular matrix. *J. Mol. Biol.* **425**, 4286–4294 (2013).

220. Thongsomboon, W. et al. Phosphoethanolamine cellulose: a naturally produced chemically modified cellulose. *Science* **359**, 334–338 (2018).

221. Rossini, A. J. et al. Dynamic nuclear polarization NMR spectroscopy of microcrystalline solids. *J. Am. Chem. Soc.* **134**, 16899–16908 (2012).

222. Hartman, J. D., Day, G. M. & Beran, G. J. Enhanced NMR discrimination of pharmaceutically relevant molecular crystal forms through fragment-based ab initio chemical shift predictions. *Cryst. Growth Des.* **16**, 6479–6493 (2016).

223. Lu, X. et al. Molecular interactions in posaconazole amorphous solid dispersions from two-dimensional solid-state NMR spectroscopy. *Mol. Pharm.* **16**, 2579–2589 (2019).

224. Nilsson Lill, S. O. et al. Elucidating an amorphous form stabilization mechanism for tenapanor hydrochloride: crystal structure analysis using X-ray diffraction, NMR crystallography, and molecular modeling. *Mol. Pharm.* **15**, 1476–1487 (2018).

225. Leclaire, J. et al. Structure elucidation of a complex CO_2-based organic framework material by NMR crystallography. *Chem. Sci.* **7**, 4379–4390 (2016).

226. Hofstetter, A. et al. Rapid structure determination of molecular solids using chemical shifts directed by unambiguous prior constraints. *J. Am. Chem. Soc.* **141**, 16624–16634 (2019).

227. Engel, E. A. et al. A Bayesian approach to NMR crystal structure determination. *Phys. Chem. Chem. Phys.* **21**, 23385–23400 (2019).

228. Ni, Q. Z. et al. In situ characterization of pharmaceutical formulations by dynamic nuclear polarization enhanced MAS NMR. *J. Phys. Chem. B* **121**, 8132–8141 (2017).

229. Walder, B. J. et al. One- and two-dimensional high-resolution NMR from flat surfaces. *ACS Cent. Sci.* **5**, 515–523 (2019).

230. Webber, A. L. et al. Identifying guanosine self assembly at natural isotopic abundance by high-resolution H-1 and C-13 solid-state NMR spectroscopy. *J. Am. Chem. Soc.* **133**, 19777–19795 (2011).

231. Mann, S. K., Pham, T. N., McQueen, L. L., Lewandowski, J. R. & Brown, S. P. Revealing intermolecular hydrogen bonding structure and dynamics in a deep eutectic pharmaceutical by magic-angle spinning NMR spectroscopy. *Mol. Pharm.* **17**, 622–631 (2020).

232. Jiang, X. et al. Thermally activated transient dipoles and rotational dynamics of hydrogen-bonded and charge-transferred diazabicyclo 2.2.2 octane molecular rotors. *J. Am. Chem. Soc.* **141**, 16802–16809 (2019).

233. Tracht, U. et al. Length scale of dynamic heterogeneities at the glass transition determined by multidimensional nuclear magnetic resonance. *Phys. Rev. Lett.* **81**, 2727–2730 (1998).

234. Viger-Gravel, J. et al. Structure of lipid nanoparticles containing siRNA or mRNA by dynamic nuclear polarization-enhanced NMR spectroscopy. *J. Phys. Chem. B* **122**, 2073–2081 (2018).

235. Pinon, A. C., Skantze, U., Viger-Gravel, J., Schantz, S. & Emsley, L. Core-shell structure of organic crystalline nanoparticles determined by relayed dynamic nuclear polarization NMR. *J. Phys. Chem. A* **122**, 8802–8807 (2018).

236. Johnson, R. L. & Schmidt-Rohr, K. Quantitative solid-state ¹³C NMR with signal enhancement by multiple cross polarization. *J. Magn. Reson.* **239**, 44–49 (2014).

237. Mao, J. D., Cao, X. Y., Olk, D. C., Chu, W. Y. & Schmidt-Rohr, K. Advanced solid-state NMR spectroscopy of natural organic matter. *Prog. Nucl. Magn. Reson. Spect.* **100**, 17–51 (2017).

238. Mao, J. D. et al. Abundant and stable char residues in soils: implications for soil fertility and carbon sequestration. *Environ. Sci. Technol.* **46**, 9571–9576 (2012).

239. Duan, P. et al. The chemical structure of carbon nanothreads analyzed by advanced solid-state NMR. *J. Am. Chem. Soc.* **140**, 7658–7666 (2018).

240. Hu, Y. Y., Rawal, A. & Schmidt-Rohr, K. Strongly bound citrate stabilizes the apatite nanocrystals in bone. *Proc. Natl Acad. Sci. USA* **107**, 22425–22429 (2010).
This study employs ¹³C chemical shifts and ¹³C–³¹P distance NMR spectroscopy experiments to show that the calcium phosphate surfaces in bone are studded with citrate molecules, which stabilize the apatite nanocrystals in bone.

241. Davies, E. et al. Citrate bridges between mineral platelets in bone. *Proc. Natl Acad. Sci. USA* **111**, E1354–E1363 (2014).

242. Moran, R. F. et al. Ensemble-based modeling of the NMR spectra of solid solutions: cation disorder in $Y_2(Sn,Ti)_2O_7$. *J. Am. Chem. Soc.* **141**, 17838–17846 (2019).

243. Ashbrook, S. E. et al. New insights into phase distribution, phase composition and disorder in $Y_2(Zr,Sn)_2O_7$ ceramics from NMR spectroscopy. *Phys. Chem. Chem. Phys.* **17**, 9049–9059 (2015).

244. Valla, M. et al. Atomic description of the interface between silica and alumina in aluminosilicates through dynamic nuclear polarization surface-enhanced NMR spectroscopy and first-principles calculations. *J. Am. Chem. Soc.* **137**, 10710–10719 (2015).

245. Playford, H. Y. et al. Characterization of structural disorder in γ-Ga_2O_3. *J. Phys. Chem. C* **118**, 16188–16198 (2014).

246. Jaegers, N. R., Mueller, K. T., Wang, Y. & Hu, J. Z. Variable temperature and pressure operando MAS NMR for catalysis science and related materials. *Acc. Chem. Res.* **53**, 611–619 (2020).

247. Buannic, L., Blanc, F., Middlemiss, D. S. & Grey, C. P. Probing cation and vacancy ordering in the dry and hydrated yttrium-substituted $BaSnO_5$ perovskite by NMR spectroscopy and first principles calculations: implications for proton mobility. *J. Am. Chem. Soc.* **134**, 14483–14498 (2012).

248. Alharbi, E. A. et al. Atomic-level passivation mechanism of ammonium salts enabling highly efficient perovskite solar cells. *Nat. Commun.* **10**, 3008 (2019).

249. Kubicki, D. J. et al. Phase segregation in Cs-, Rb- and K-doped mixed-cation $(MA)_x(FA)_{1−x}PbI_3$ hybrid perovskites from solid-state NMR. *J. Am. Chem. Soc.* **139**, 14173–14180 (2017).

250. Soleilhavoup, A., Hampson, M. R., Clark, S. J., Evans, J. S. O. & Hodgkinson, P. Using O-17 solid-state NMR and first principles calculation to characterise structure and dynamics in inorganic framework materials. *Magn. Reson. Chem.* **45**, S144–S155 (2007).

251. Pecher, O., Carretero-Gonzalez, J., Griffith, K. J. & Grey, C. P. Materials' methods: NMR in battery research. *Chem. Mater.* **29**, 213–242 (2017).

252. Liu, T. et al. Cycling Li-O_2 batteries via LiOH formation and decomposition. *Science* **350**, 530–533 (2015).
This paper describes how to overcome key challenges in engineering of lithium–air batteries and the use of ⁷Li and ¹H NMR spectroscopy to determine the discharge products and elucidate the origin of protons in the formed LiOH.

253. Chen, J. et al. Polar surface structure of oxide nanocrystals revealed with solid-state NMR spectroscopy. *Nat. Commun.* **10**, 5420 (2019).

254. Stebbins, J. F. & Xue, X. Y. in *Spectroscopic Methods in Mineralogy and Materials Sciences* Vol. 78 (eds. Henderson, G. S., Neuville, D. R. & Downs, R. T.) 605–653 (Mineralogical Society of America, 2014).

255. Griffin, J. M. & Ashbrook, S. E. Solid-state NMR of high-pressure silicates in the earth's mantle. *Annu. Rep. NMR Spec.* **79**, 241–332 (2013).

256. Langner, R., Fechtelkord, M., Garcia, A., Palin, E. J. & Lopez-Solano, J. Aluminum ordering and clustering in Al-rich synthetic phlogopite: {H-1}→Si-29 CPMAS HETCOR spectroscopy and atomistic calculations. *Am. Mineral.* **97**, 341–352 (2012).

257. Florian, P., Veron, E., Green, T. F. G., Yates, J. R. & Massiot, D. Elucidation of the Al/Si ordering in gehlenite $Ca_2Al_2SiO_7$ by combined Si-29 and Al-27 NMR spectroscopy/quantum chemical calculations. *Chem. Mater.* **24**, 4068–4079 (2012).

258. Palke, A. C., Stebbins, J. F., Geiger, C. A. & Tippelt, G. Cation order–disorder in Fe-bearing pyrope and grossular garnets: a Al-27 and Si-29 MAS NMR and Fe-57 Mossbauer spectroscopy study. *Am. Mineral.* **100**, 536–547 (2015).

259. Gan, Z. H. Isotropic NMR spectra of half-integer quadrupolar nuclei using satellite transitions and magic-angle spinning. *J. Am. Chem. Soc.* **122**, 3242–3243 (2000).

260. Ashbrook, S. E. & Wimperis, S. High-resolution NMR of quadrupolar nuclei in solids: the satellite-transition magic angle spinning (STMAS) experiment. *Prog. Nucl. Magn. Reson. Spectrosc.* **45**, 53–108 (2004).

261. McKay, D. et al. A picture of disorder in hydrous wadsleyite — under the combined microscope of solid-state NMR spectroscopy and Ab initio random structure searching. *J. Am. Chem. Soc.* **141**, 3024–3036 (2019).

262. Griffin, J. M., Berry, A. J., Frost, D. J., Wimperis, S. & Ashbrook, S. E. Water in the earth's mantle: a solid-state NMR study of hydrous wadsleyite. *Chem. Sci.* **4**, 1523–1538 (2013).

263. Ashbrook, S. E., Dawson, D. M. & Seymour, V. R. Recent developments in solid-state NMR spectroscopy of crystalline microporous materials. *Phys. Chem. Chem. Phys.* **16**, 8223–8242 (2014).

264. Pugh, S. M., Wright, P. A., Law, D. J., Thompson, N. & Ashbrook, S. E. Facile, room-temperature O-17 enrichment of zeolite frameworks revealed by solid-state NMR spectroscopy. *J. Am. Chem. Soc.* **142**, 900–906 (2020).

265. Bignami, G. P. M. et al. Synthesis, isotopic enrichment, and solid-state NMR characterization of zeolites derived from the assembly, disassembly, organization, reassembly process. *J. Am. Chem. Soc.* **139**, 5140–5148 (2017).

266. Nagashima, H. et al. Recent developments in NMR studies of aluminophosphates. *Annu. Rep. NMR Spectrosc.* **94**, 113–185 (2018).

267. Dawson, D. M. et al. A multinuclear NMR study of six forms of AlPO-34: structure and motional broadening. *J. Phys. Chem. C* **121**, 1781–1793 (2017).

268. Lucier, B. E. G., Chen, S. S. & Huang, Y. N. Characterization of metal–organic frameworks: unlocking the potential of solid-state NMR. *Acc. Chem. Res.* **51**, 319–330 (2018).

269. Witherspoon, V. J., Xu, J. & Reimer, J. A. Solid-state NMR investigations of carbon dioxide gas in metal–organic frameworks: insights into molecular motion and adsorptive behavior. *Chem. Rev.* **118**, 10033–10048 (2018).

270. Kong, X. Q. et al. Mapping of functional groups in metal–organic frameworks. *Science* **341**, 882–885 (2013).
This paper shows how solid-state NMR combined with molecular simulations can map the spatial distributions of linkers in multivariate metal–organic framework materials as random, well-mixed or clustered.

271. Bonhomme, C., Gervais, C. & Laurencin, D. Recent NMR developments applied to organic–inorganic materials. *Prog. Nucl. Magn. Reson. Spectrosc.* **77**, 1–48 (2014).

272. Eden, M. ²⁷Al NMR studies of aluminosilicate glasses. *Annu. Rep. NMR Spectrosc.* **86**, 237–331 (2015).

273. Pustovgar, E. et al. Understanding silicate hydration from quantitative analyses of hydrating tricalcium silicates. *Nat. Commun.* **7**, 10952 (2016).

274. Kunhi Mohamed, A. et al. The atomic-level structure of cementitious calcium aluminate silicate hydrate. *J. Am. Chem. Soc.* **142**, 11060–11071 (2020).

275. Gervais, C., Bonhomme, C. & Laurencin, D. Recent directions in the solid-state NMR study of synthetic and natural calcium phosphates. *Solid State Nucl. Magn. Reson.* **107**, 101663 (2020).

276. Casabianca, L. B. Solid-state nuclear magnetic resonance studies of nanoparticles. *Solid State Nucl. Magn. Reson.* **107**, 101664 (2020).

277. Al-Johani, H. et al. The structure and binding mode of citrate in the stabilization of gold nanoparticles. *Nat. Chem.* **9**, 890–895 (2017).

278. Berrettini, M. G., Braun, G., Hu, J. G. & Strouse, G. F. NMR analysis of surfaces and interfaces in 2-nm CdSe. *J. Am. Chem. Soc.* **126**, 7063–7070 (2004).

279. Avenier, P. et al. Dinitrogen dissociation on an isolated surface tantalum atom. *Science* **317**, 1056–1060 (2007).

280. Trebosc, J., Wiench, J. W., Huh, S., Lin, V. S. Y. & Pruski, M. Studies of organically functionalized mesoporous silicas using heteronuclear solid-state correlation NMR spectroscopy under fast magic angle spinning. *J. Am. Chem. Soc.* **127**, 7587–7593 (2005).

281. Wang, M. et al. Identification of different oxygen species in oxide nanostructures with ^{17}O solid-state NMR spectroscopy. *Sci. Adv.* **1**, e1400133 (2015).

282. Berruyer, P. et al. Three-dimensional structure determination of surface sites. *J. Am. Chem. Soc.* **139**, 849–855 (2017).

283. Kobayashi, T., Perras, F. A., Slowing, I. I., Sadow, A. D. & Pruski, M. Dynamic nuclear polarization solid-state NMR in heterogeneous catalysis research. *ACS Catal.* **5**, 7055–7062 (2015).

284. Perras, F. A., Wang, Z. R., Naik, P., Slowing, I. I. & Pruski, M. Natural abundance O-17 DNP NMR provides precise O–H distances and insights into the bronsted acidity of heterogeneous catalysts. *Angew. Chem. Int. Ed.* **56**, 9165–9169 (2017).

285. Tošner, Z. et al. Overcoming volume selectivity of dipolar recoupling in biological solid-state NMR spectroscopy. *Angew. Chem. Int. Ed. Engl.* **57**, 14514–14518 (2018).

286. Lewandowski, J. R., De Paëpe, G. & Griffin, R. G. Proton assisted insensitive nuclei cross polarization. *J. Am. Chem. Soc.* **129**, 728–729 (2007).

287. Samoson, A. H-MAS. *J. Magn. Res.* **306**, 167–172 (2019).

288. Wang, Z. et al. Combining fast magic angle spinning dynamic nuclear polarization with indirect detection to further enhance the sensitivity of solid-state NMR spectroscopy. *Solid State Nucl. Magn. Reson.* **109**, 101685 (2020).

289. Tycko, R. & Hu, K. N. A Monte Carlo/simulated annealing algorithm for sequential resonance assignment in solid state NMR of uniformly labeled proteins with magic-angle spinning. *J. Magn. Reson.* **205**, 304–314 (2010).

290. Fritzsching, K. J., Yang, Y., Schmidt-Rohr, K. & Hong, M. Practical use of chemical shift databases for protein solid-state NMR: 2D chemical shift maps and amino-acid assignment with secondary-structure information. *J. Biomol. NMR* **56**, 155–167 (2013).

291. Fritzsching, K. J., Hong, M. & Schmidt-Rohr, K. Conformationally selective multidimensional chemical shift ranges in proteins from a PACSY database purged using intrinsic quality criteria. *J. Biomol. NMR* **64**, 115–130 (2016).

292. Yang, Y., Fritzsching, K. J. & Hong, M. Resonance assignment of disordered proteins using a multi-objective non-dominated sorting genetic algorithm. *J. Biomol. NMR* **57**, 281–296 (2013).

293. Bartok, A. P. & Yates, J. R. Regularized SCAN functional. *J. Chem. Phys.* **150**, 207101 (2019).

294. Hartman, J. D., Kudla, R. A., Day, G. M., Mueller, L. J. & Beran, G. J. Benchmark fragment-based ^{1}H, ^{13}C, ^{15}N and [17]O chemical shift predictions in molecular crystals. *Phys. Chem. Chem. Phys.* **18**, 21686–21709 (2016).

295. Paruzzo, F. M. et al. Chemical shifts in molecular solids by machine learning. *Nat. Commun.* **9**, 4501 (2018).

296. Iwasa, Y. et al. A high-resolution 1.3-GHz/54-mm LTS/HTS NMR magnet. *IEEE Trans. Appl. Supercond.* **25**, 1–5 (2015).

297. Gan, Z. et al. NMR spectroscopy up to 35.2 T using a series-connected hybrid magnet. *J. Magn. Reson.* **284**, 125–136 (2017).

298. Xue, K. et al. Impact of magnetic field strength on resolution and sensitivity of proton resonances in biological solids. *J. Phys. Chem. C.* **124**, 22631–22637 (2020).

299. Keeler, E. G. et al. ^{17}O MAS NMR correlation spectroscopy at high magnetic fields. *J. Am. Chem. Soc.* **139**, 17953–17963 (2017).

300. Chen, P. H. et al. Magic angle spinning spheres. *Sci. Adv.* **4**, eaau1540 (2018).

301. Agarwal, V. et al. De novo 3D structure determination from sub-milligram protein samples by solid-state 100 kHz MAS NMR spectroscopy. *Angew. Chem. Int. Ed.* **53**, 12253–12256 (2014).

302. Xue, K. et al. Magic angle spinning frequencies beyond 300 kHz are necessary to yield maximum sensitivity in selectively methyl protonated protein samples in solid state NMR. *J. Phys. Chem. C* **122**, 16437–16442 (2018).

303. Gao, C. et al. Four millimeter spherical rotors spinning at 28 kHz with double-saddle coils for cross polarization NMR. *J. Magn. Reson.* **303**, 1–6 (2019).

304. Berruyer, P. et al. Dynamic nuclear polarization enhancement of 200 at 21.15 T enabled by 65 kHz magic angle spinning. *J. Phys. Chem. Lett.* **11**, 8386–8391 (2020).

305. Can, T. V., Walish, J. J., Swager, T. M. & Griffin, R. G. Time domain DNP with the NOVEL sequence. *J. Chem. Phys.* **143**, 054201 (2015).

306. Jaudzems, K. et al. Dynamic nuclear polarization-enhanced biomolecular NMR spectroscopy at high magnetic field with fast magic-angle spinning. *Angew. Chem. Int. Ed.* **57**, 7458–7462 (2018).

307. Tosner, Z. et al. Optimal control in NMR spectroscopy: numerical implementation in SIMPSON. *J. Magn. Res.* **197**, 120–134 (2009).

308. Concistrè, M., Johannessen, O. G., Carignani, E., Geppi, M. & Levitt, M. H. Magic-angle spinning NMR of cold samples. *Acc. Chem. Res.* **46**, 1914–1922 (2013).

309. Jeon, J., Thurber, K. R., Ghirlando, R., Yau, W. M. & Tycko, R. Application of millisecond time-resolved solid state NMR to the kinetics and mechanism of melittin self-assembly. *Proc. Natl Acad. Sci. USA* **116**, 16717–16722 (2019).

310. Freedberg, D. I. & Selenko, P. Live cell NMR. *Annu. Rev. Biophys.* **43**, 171–192 (2014).

311. Chow, W. Y. et al. NMR spectroscopy of native and in vitro tissues implicates polyADP ribose in biomineralization. *Science* **344**, 742–746 (2014).

312. Narasimhan, S. et al. DNP-supported solid-state NMR spectroscopy of proteins inside mammalian cells. *Angew. Chem. Int. Ed.* **58**, 12969–12973 (2019).

313. Jacso, T. et al. Characterization of membrane proteins in isolated native cellular membranes by dynamic nuclear polarization solid-state NMR spectroscopy without purification and reconstitution. *Angew. Chem. Int. Ed.* **51**, 432–435 (2012).

314. Kaplan, M. et al. EGFR dynamics change during activation in native membranes as revealed by NMR. *Cell* **167**, 1241–1251 (2016).

315. Yusa, G., Muraki, K., Takashina, K., Hashimoto, K. & Hirayama, Y. Controlled multiple quantum coherences of nuclear spins in a nanometre-scale device. *Nature* **434**, 1001–1005 (2005).

316. Meriles, C. A. et al. High-resolution NMR of static samples by rotation of the magnetic field. *J. Magn. Reson.* **169**, 13–18 (2004).

317. Sakellariou, D. et al. Permanent magnet assembly producing a strong tilted homogeneous magnetic field: towards magic angle field spinning NMR and MRI. *Magn. Reson. Chem.* **48**, 903–908 (2010).

318. Niu, Z. et al. Mapping of the binding interface of PET tracer molecules and Alzheimer disease Aβ fibrils using MAS solid-state NMR. *ChemBioChem* **21**, 2495–2502 (2020).

319. Reichert, D. & Krushelnitsky, A. in *Modern Methods in Solid-state NMR: A Practitioner's Guide* (ed. Hodgkinson, P.) (RSC, 2018).

320. Ashbrook, S. E. et al. ^{17}O and ^{29}Si NMR parameters of MgSiO$_3$ phases from high-resolution solid-state NMR spectroscopy and first-principles calculations. *J. Am. Chem. Soc.* **129**, 13213–13224 (2007).

321. Haw, J. F., Song, W., Marcus, D. M. & Nicholas, J. B. The mechanism of methanol to hydrocarbon catalysis. *Acc. Chem. Res.* **36**, 317–326 (2003).

322. Alanazi, A. Q. et al. Atomic-level microstructure of efficient formamidinium-based perovskite solar cells stabilized by 5-ammonium valeric acid iodide revealed by multinuclear and two-dimensional solid-state NMR. *J. Am. Chem. Soc.* **141**, 17659–17669 (2019).

323. Martins, V. et al. Higher magnetic fields, finer MOF structural information: ^{17}O solid-state NMR at 35.2 T. *J. Am. Chem. Soc.* **142**, 14877–14889 (2020).

324. Paravastu, A.K. Leapman, R.D., Yau, W.M, Tycko, R. Molecular structural basis for polymorphism in Alzheimer's beta-amyloid fibrils. *Proc. Natl Acad. Sci. USA* **105**, 18349–18354 (2008).

Author contributions
Introduction (B.R., S.E.A., L.E. and M.H.); Experimentation (B.R., S.E.A., L.E. and M.H.); Results (B.R., S.E.A., L.E. and M.H.); Applications (B.R., S.E.A., L.E. and M.H.); Reproducibility and data deposition (B.R., S.E.A., L.E. and M.H.); Limitations and optimizations (B.R., S.E.A., L.E. and M.H.); Outlook (B.R., S.E.A., L.E. and M.H.); overview of the Primer (M.H.).

Competing interests
The authors declare no competing interests.

Publisher's note
Springer Nature remains neutral with regard to jurisdictional claims in published maps and institutional affiliations.

RELATED LINKS
Biological Magnetic Resonance Data Bank (BRMB): https://bmrb.io/
Cambridge Structural Database (CSD): https://www.ccdc.cam.ac.uk/solutions/csd-system/components/csd/
Inorganic Crystal Structure Database (ICSD): https://icsd.products.fiz-karlsruhe.de
Protein Databank (PDB): https://www.rcsb.org/